*International Geology Review*, Vol. 46, 2004, p. XXX–XXX.


# Petrology and Chemistry of Metasomatic Blocks from Bawshir, Northeastern Oman

ALEY K. EL-SHAZLY

*Department of Geology, Geography, and Physics, University of Tennessee, Martin, Tennessee 38238*

AND MOHAMMED AL-BELUSHI

*Ministry of Oil and Gas, P.O. Box 551, PC 113, Muscat, Sultanate of Oman*

## Abstract

Several types of Ca-rich, metasomatically altered rocks occur as blocks or reaction zones in a serpentinite-matrix mélange in the Bawshir–Al-Khuwair area, west of Ruwi in northeastern Oman. Type A rodingites contain mainly hydrogarnet, with smaller amounts of diopside, tremolite ± pumpellyite ± prehnite. Type B rocks contain more diopside ± tremolite and smaller amounts of hydrogarnet. Type C nephrites consist chiefly of tremolite and have a distinctive botryoidal texture. Quartzite blocks in this mélange were also affected by Ca-metasomatism, and contain variable amounts of tremolite, hydrogarnet, chlorite, and clinozoisite.

Relatively immobile trace and rare-earth element contents of these rocks suggest that the protoliths of types A and B metasomatic rocks were ocean-island basalts, whereas type C nephrites represent metasomatized serpentinites. Isocon diagrams show that all metasomatic rocks formed by the addition of Ca ± Mg ± volatiles, and leaching of almost all other elements to variable degrees. Field and textural relations interpreted with an activity-corrected petrogenetic grid in the system CMASH suggest that metasomatism took place in stages over a range of P-T conditions, beginning at 220–310°C and 3–6 kbar, and ending at 250–310°C, $P < 3.2$ kbar. Diffusion of $Ca^{2+}$ out of the serpentinizing peridotites into blocks of basalts and quartzites was the primary cause of early metasomatism, which overlapped with high P/T metamorphism of the same blocks. Infiltration of low-salinity aqueous fluids was partly responsible for the latest stages of metasomatism, which took place during exhumation, and continued after the final emplacement of the ophiolite.

## Introduction[1]

A COMMON PHENOMENON at the contacts between serpentinized ultramafic bodies and other rock types is Ca-metasomatism, which results in the formation of rodingites and nephrites (e.g., Coleman, 1967; Honnorez and Kirst, 1975; Capedri et al, 1978; Barriga and Fyfe, 1983). These metasomatic rocks usually occur as blocks, dikes, veins, selvages, or reaction fronts (e.g., Coleman, 1967). Although Ca-metasomatites are fairly common, their petrogenesis is poorly understood, and the source and composition of metasomatic fluids involved in their formation are still debated. Mechanisms suggested for the formation of these rocks include: (1) alteration of gabbroic rocks either by late-magmatic hydrothermal fluids (Bilgrami and Howie, 1960; Qaiser et al., 1970) or seawater (e.g., Hall and Ahmed, 1984); (2) metasomatism associated with high-temperature serpentinization (> 300°C) at significant depths (e.g., Honnorez and Kirst, 1975; Wenner, 1979); (3) metasomatism accompanying "ocean-floor metamorphism" and later tectonic emplacement of oceanic lithosphere, both concomitant with serpentinization of ultramafics (e.g., Capedri et al., 1978); and (4) metasomatism associated with low-temperature serpentinization following the emplacement of ultramafic rocks (e.g., Coleman, 1967; Barnes and O'Neil, 1969; Wenner, 1979; Barriga and Fyfe, 1983; Prokhor, 1991).

[1]Abbreviations used in this paper are as follows: Act = actinolite; Ap = apatite, Cc = calcite, Chl = chlorite, Chr = chromite; Cpx = clinopyroxene; Czo = clinozoisite; Di = diopside, Dol = dolomite; E-MORB = enriched mid-ocean ridge basalts; Ep = epidote, $Fe_2O_3$* = total Fe-oxides expressed as $Fe_2O_3$, Gr = grossular; Gt = garnet, Mc = magnesite; Mgt = magnetite; Qz = quartz; Tc = talc; Hgt = hydrogarnet; Hrc = hercynite; Ill = illite; Jd = jadeite, Lw = lawsonite; OIB = ocean-island basalt; Ol = olivine; Opq = opaque phase; Opx = orthopyroxene; Oxychl = oxychlorite; Plag = plagioclase feldspar; Pmp = pumpellyite; Prh = prehnite; Sp = spinel; Srp = serpentine; Tc = talc; Tr = tremolite; Ttn = titanite.

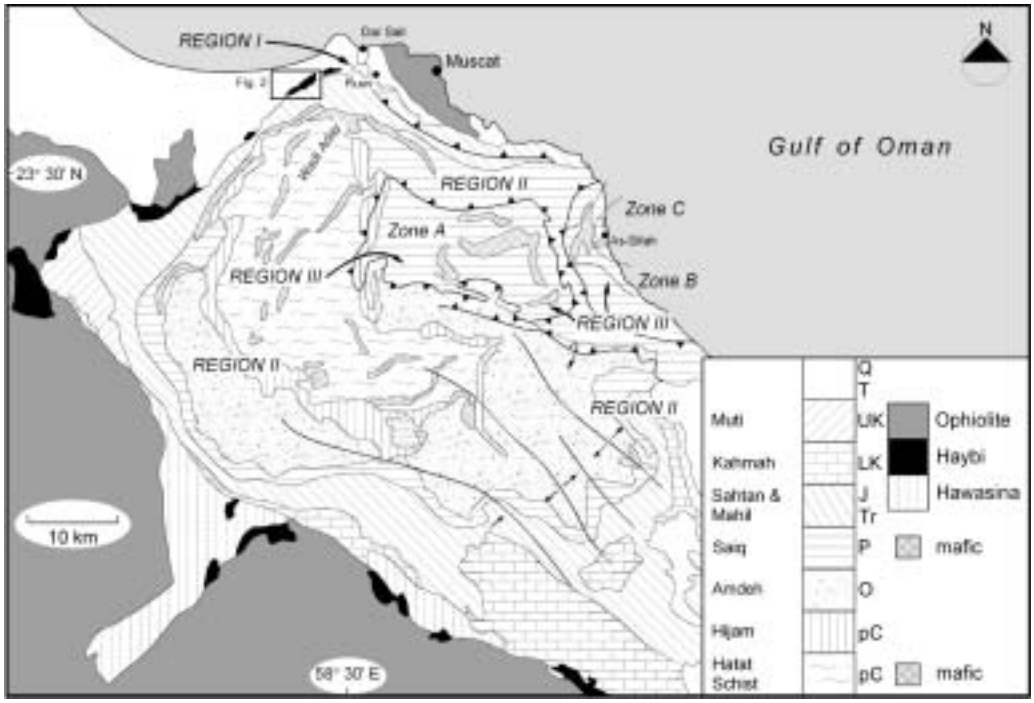


FIG. 1. Geological map of Saih Hatat, northeastern Oman, simplified after Le Métour et al. (1986) and Gregory et al. (1998). Regions I, II, and III and metamorphic zones A, B, and C are from El-Shazly and Coleman (1990). The right-hand key represents the allochthonous units, whereas the left-hand key represents the autochthonous and parautochthonous basement, shelf, and foreland basin units. Abbreviations: Q = Quaternary; T = Tertiary; K = Cretaceous; Tr = Triassic; J = Jurassic; P = Permian; pC = Precambrian. The area enclosed in a box is that shown in Figure 2.

Rodingites and nephrites occur as blocks or reaction zones around blocks enclosed in a serpentinite-matrix mélange in the Bawshir–Al-Khuwair area, on the northwest flanks of Saih Hatat, northeast Oman (Fig. 1). This mélange is part of a unit sandwiched between parautochthonous continental shelf rocks metamorphosed under high-pressure, low-temperature (high P/T) conditions, and the allochthonous Semail ophiolite and Hawasina complex. The origin of this mélange and its relation to the emplacement of the Semail ophiolite and high-P/T metamorphism are poorly understood. Glennie et al. (1974) mapped this serpentinite matrix mélange as part of the "Oman Mélange/Exotics," a mélange with Permian to Triassic carbonate blocks formed on horsts or seamounts in the distal portions of the Hawasina basin. Le Métour et al. (1986) considered it part of the Upper Cretaceous Muti Formation, a syntectonic foreland basin unit deposited during emplacement of the ophiolite. Other mélanges in areas such as Fanjah, Bid Bid, and northern Oman, having similar structural positions to the serpentinite matrix mélange, have been mapped as part of the Hawasina complex (e.g., Villey et al., 1986), in line with Glennie et al.'s (1974) interpretation.

This preliminary petrological and geochemical study is aimed at: (1) documenting the field and petrographic characteristics of metasomatic rocks from the serpentinite matrix mélange and their relations to the surrounding units; (2) determining the conditions and mechanisms of metasomatism; (3) identifying the source of metasomatic fluids; and (4) understanding the mode of formation of the serpentinite matrix mélange and its relationship to high P/T metamorphism in Saih Hatat, ophiolite emplacement, and/or serpentinization.

## Geologic Setting and Field Relations

The Saih Hatat area is a tectonic window that exposes basement and shelf units structurally

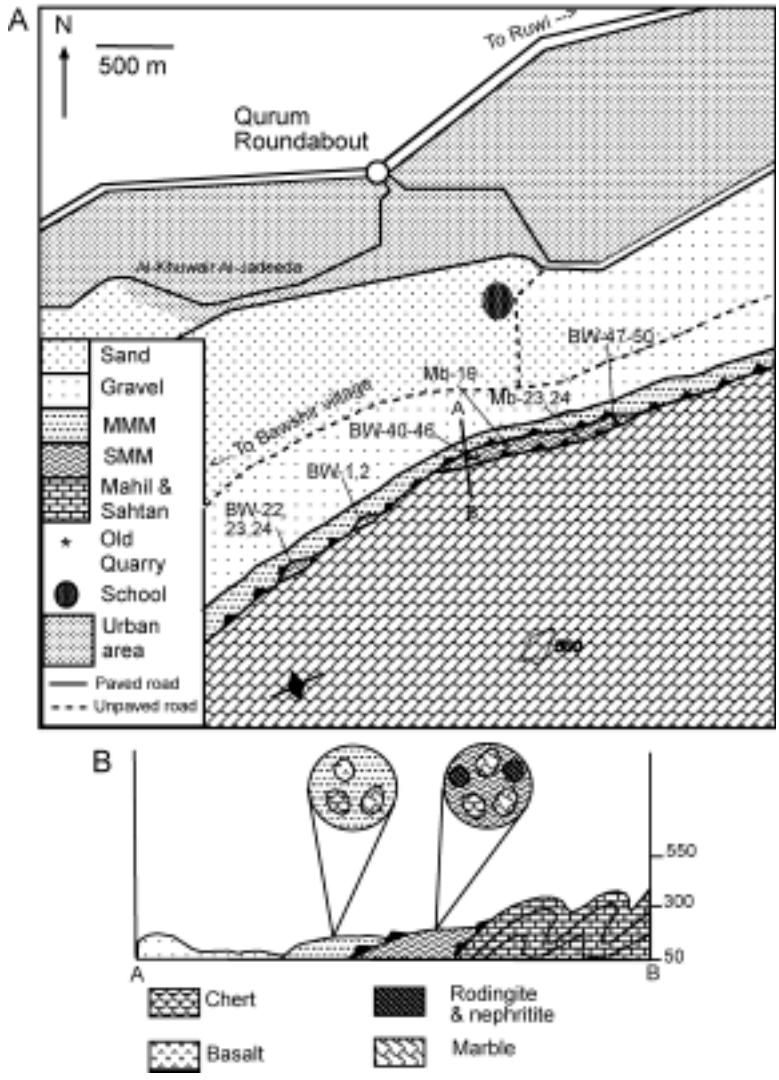


FIG. 2. A. Geological map of the Bawshir–Al-Khuwair area showing the locations of selected samples described in this study. B. Cross section along line A–B of Figure 2A.

underlying the allochthonous Semail ophiolite, Haybi complex, and Hawasina basin complex (Fig. 1). The basement and shelf units were variably affected by high P/T metamorphism during emplacement of the Semail ophiolite (e.g., Le Métour et al., 1990; El-Shazly et al., 2001). The Bawshir–Al-Khuwair area is located about 25 km west of Muscat on the northwestern flank of the Saih Hatat dome (Fig. 1). It consists of Mesozoic shelf carbonates overthrust by a serpentinite-matrix mélange (SMM) that is in turn overthrust by a metamorphosed muddy-matrix mélange (MMM) partly covered by sand dunes and gravels (Figs. 2 and 3). Both mélanges are collectively termed "the sandwich horizon" (Coleman, pers. commun., 1998).

The shelf carbonates are folded into tight folds with ENE-WSW–striking axial planes. They were all metamorphosed under pumpellyite-actinolite to epidote–blueschist facies conditions (El-Shazly, 1994). The SMM is discontinuous along strike. It consists of intensely sheared serpentinites with pods and veins of magnesite enclosing blocks of marble,

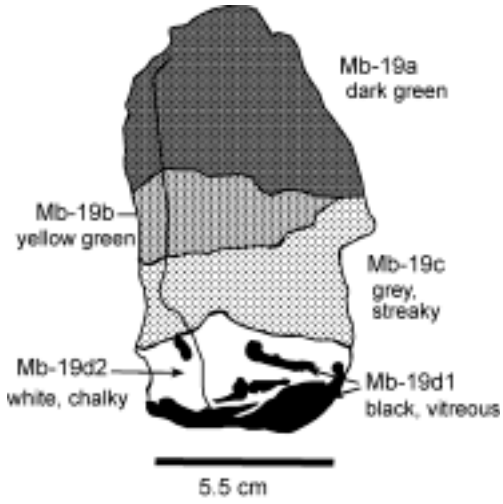


FIG. 3. Schematic sketch of sample Mb-19a–d, showing the different metasomatic zones and fronts. Mineral assemblages of each zone are given in Table 2.

quartzite (metachert), nephrite, and rodingite. Red and grey phyllites of the MMM are thrust onto the SMM (Figs. 2A and 2B), and in turn contain blocks of marble, metabasalt, and chert. Although they too are discontinuous along strike, they occupy the same structural position as the Ruwi mélange, exposed in the Ruwi–Hamiriya–Darsait areas, and containing high-P/T mineral assemblages characteristic of the lawsonite albite facies (e.g., Goffé et al., 1988; El-Shazly, 1995, 1996; Fig. 1). A summary of the field relations in these three areas is given in Table 1.

Three types of metasomatic rocks (types A, B and C) were identified in the study area. Type A metasomatites are defined as those rocks in which garnet or hydrogarnet is the most abundant phase (constituting as much as 70% of the rock by volume) and are therefore "rodingites." These rocks are reddish brown, white or light green in color, very hard and massive, and occur mostly as rinds or reaction zones on other types of blocks. They are always in contact with serpentinites. The most common mineral assemblage in type A rodingites is Hgt–Di–Tr (Table 2). Secondary prehnite, chlorite, carbonates (calcite, magnesite or dolomite) ± talc are also present. Type B metasomatites consist principally of diopside and/or tremolite. They are very fine grained, pale green to chalky white, massive, strong, and dense blocks or reaction zones that are typically separated from the serpentinites by a zone of type A or C rocks. The most common mineral assemblage in this rock type is Di–Hgt–Tr ± Plag ± Pmp ± Chl. Type C metasomatites are white to greenish nephrites with a characteristic botryoidal texture, and appear to have replaced some of the serpentinites with which they are in contact. These nephrites are chiefly tremolite ($\geq$ 50 modal %) with small amounts of Hgt and Fe-oxides (Table 2). In addition to these three metasomatic rock types, some quartzites (metacherts) and a calcareous schist show signs of "Ca-metasomatism." The metasomatized quartzites contain variable amounts of tremolite, hydrogranet, Fe-oxides, chlorite, sericite, epidote/ clinozoisite, titanite, plagioclase, and calcite. Most samples are brecciated or sheared; these breccia zones are filled with coarser grained (recrystallized?) quartz, clusters of fibrous

TABLE 1: Field Relations of the Sandwich Horizon, Saih Hatat Area

| Locality: Unit | Bawshir–Al-Kuwair | Darsait–Ruwi | Ruwi–Hamiriya | Stratigraphic unit |
|---|---|---|---|---|
| Ophiolite | – | Dunite | – | Semail ophiolite |
| Mélange | – | Serpentinite + chert + basalt | – | Hawasina? |
| Muddy matrix Mélange (MMM) | Red and grey phyllite with blocks of marble and chert | Red and grey phyllite + Fe-carpholite schist + Lw schist with blocks of metabasalt and marble | Red and grey phyllite + Fe-carpholite schist + Lw schist with blocks of metabasalt + marble + serpentinite | Muti or Hawasina? |
| Serpentinite-matrix Mélange (SMM) | Blocks of marble + chert + rodingite + nephritite | Serpentinite; no blocks | – | Muti or Hawasina? |
| Shelf units | Sahtan | Sahtan | Sahtan | Sahtan |

TABLE 2. Mineral Modes for Selected Samples[1]

| Sample | Type | Hgt | Di | Tr | Prh | Chl | Opq | Cc | Plag | Srp | Others |
|---|---|---|---|---|---|---|---|---|---|---|---|
| BW-2 | A | 65 | – | 5 | 20 | 5 | tr | – | | tr | Tc (5), Ttn (tr) |
| BW-23 | A | 65 | tr? | ? | – | 5 | 3 | Mc (5) | – | 20 | – |
| BW-18a | A | 35–40 | 35 | 10 | 15–20 | – | 5 | – | – | 5 | Epistilbite (5) |
| Mb-19c | A | 65 | 25 | 5 | – | – | tr | – | 5 | – | – |
| Mb-19d1 | A/Srp | 40 | – | – | – | 15–20 | 5 | (tr) | – | 40 | |
| Mb-19d2 | A | 60 | 40 | | | | tr | | | | |
| Mb-21a | A | 70 | – | 25 | – | – | tr | – | tr | – | Oxychl (5) |
| BW-1 | B | 20–25 | 5? | 25 | – | 5 | tr | – | 10 | – | Pmp (20), Natrolite (5), Qz (5) |
| Mb-19a | B | 30 | – | 5–10 | – | 15 | 3–5 | – | 5–10 | – | Pmp (30) |
| Mb-19b | B | 25–30 | 25 | – | – | 5 | tr | – | 5 | – | Pmp (35–40), Ttn(tr) |
| BW-15 | B | 15–20 | 50 | 15–20 | – | – | tr | – | 5 | – | – |
| BW-24 | B | 15–20 | – | 20 | – | 5 | 10–15 | Mc (5) | – | 35 | Cpx (3–5) |
| BW-40 | B | 15–20 | – | 70–75 | – | 5 | 2–3 | – | – | – | – |
| BW-18b | B/Srp | 15 | – | 10 | tr | – | 10 | – | – | 65 | – |
| BW-16 | C | 5 | – | 85 | – | 10 | – | – | – | – | – |
| BW-46 | C | 3–5 | ? | 85–90 | tr? | – | 2–3 | – | – | 5 | – |
| BW-48 | C | 20 | ? | 75 | – | – | 5 | – | – | – | – |
| K-1 | C | 5 | 40 | 50 | – | – | 3–5 | – | tr? | – | – |
| BW-11 | Srp | 5 | tr | 5? | – | – | 5 | – | – | 80 | Opx, Ol |
| BW-12 | Srp | | | | | | 5 | 5 | | 80 | Opx (5), Cpx (5) |
| BW-14 | CS | – | – | 35 | – | – | 3–5 | Dol (55) | – | 5 | Tc (tr)? |
| BW-39 | Q | 5 | – | 10 | – | – | tr | 5 | – | – | Qz (80), Ep (tr) |
| BW-50 | Q | 15–20 | – | 10 | – | – | tr | – | – | – | Qz (65), Ill (5) |

[1]CS = calcareous schist; Q = quartzite; tr = traces; Ill = illite.

tremolite, garnet/hydrogarnet, chlorite, Fe-oxides, and calcite. The calcareous schist (represented by BW-14) consists of dolomite, tremolite, Fe-oxides, chlorite, and traces of talc and serpentine (Table 2), and seems to have formed at the expense of a serpentinite or ophidolomite.

Several of the samples studied display metasomatic fronts defined by distinct reaction bands. This is particularly evident around all blocks of quartzite and some rodingite blocks in the SMM that develop rinds or reaction fronts defined by two to four zones with different colors, textures, and mineral assemblages. Among these, samples BW-48 to BW-50 represent a white, botryoidal, type C nephrite (BW-48) apparently replacing serpentinite with some pseudomorphs of Tr after Opx or bastite, grading into a grey massive type B metasomatite (BW-49) that in turn grades into the quartzite block (BW-50; Table 2). The most spectacular example of such fronts is represented by samples Mb-19a–d (Fig. 3), where a "metabasaltic" block is characterized by four mineralogically distinct zones before grading into the host serpentinites (Fig. 3 and Table 2).

## Mineral and Rock Chemistry

### *Analytical techniques*

Minerals were analyzed at Sultan Qaboos University (SQU) using a JEOL 830-A SEM equipped with an EDS system including an ATW sealed window Si(Li) detector with 138 eV resolution, and accompanying LINK ISIS 300 software. EDS quantitative analysis was carried out at 20 KV with a focused (~1 µm beam). Sample current measured on Co was 34 nAmp. Detector live time was 50 seconds, with a deadtime < 25%. Calibration was carried out on the following well-characterized Smithsonian standards: scapolite (Na, Al, Cl), microcline (Si, K), Kakanui hornblende (Ti), Johnstown hypersthene (Fe), chromite (Cr), diopside (Ca, Mg), and Rockport fayalite (Mn). Matrix corrections were carried out with a ZAF-4 program (SEMQUANT). Kakanui augite and Kakanui hornblende were routinely analyzed as unknowns to check for any drift. All analyses for all calibrated oxides are considered to have a precision of 1–2% or better. X-ray diffraction was carried out on a fully automated Siemens D500 I-I powder diffractometer at University of Tennessee, Knoxville. Major- and trace-element analyses were carried out using XRF spectrometry on fused beads and ICP–MS following metaborate fusion and dissolution, both at ALS CHEMEX, Toronto, Canada. Microthermometric measurements were performed on a Fluid Inc. USGS-type gas-flow heating-freezing stage at Rice University. Analytical details are described in El-Shazly and Sisson (2004).

*Garnet and hydrogarnet*. In type A-rodingite, Hgt occurs as cloudy, weakly birefringent, framboidal crystals that grade into dense almost monomineralic aggregates (Fig. 4A) or in stellar-shaped radiating clusters, and is therefore similar to the "paragarnet" of Barriga and Fyfe (1983). In type B and C metasomatites, Gt or Hgt occur as minute (0.05–0.1 mm) granular grains with interstitial diopside or tremolite that typically have opaque cores (of Cr-spinel, e.g., K-1), or pink to reddish rims (e.g., BW-16). Aggregates of these crystals concentrate along veinlets and stringers, or in brecciated veins (e.g., BW-40, BW-23; Fig. 4B). In quartzites, hydrogarnet is a minor phase in veinlets and brecciated horizons.

The mineral formula of hydrogarnet was calculated on the basis of three fixed cations for the 12 coordinated X site (Ca, Mg, Mn) using MINFILE (Afifi and Essene, 1988), assuming all Fe as $Fe^{+3}$ and $H_2O$ = 100 – sum of all oxide wt%. This method proved to be more appropriate than calculations on the basis of 8 total cations, or 12 oxygen atoms. All $H^+$ was assigned to the tetrahedral site, which was completed to 3 assuming a site preference of $Fe^{3+}$> Al > $Ti^{+4}$ (Huggins et al., 1977), only if the apparent octahedral (Y) site occupancy exceeded 2. $Mn^{+2}$ was assigned to the octahedral site only if it contained $Ti^{+4}$. End-member components were calculated following the scheme: pyrope (prp) = all Mg, spessartine (sps) = all $Mn^{+2}$ in the X site, schorlomite (schl) = 1.5 * $Ti^{+4}$ in Y, andradite (andr) = 1.5 * $Fe^{3+}$ in Y, and grossular (grs) = 1.5($Al^{vi}$ – 2/3Mg) (Table 3). The results show that all hydrogarnets ($X_3Y_2(SiO_4)_{3-p}(H_4O_4)_p$) analyzed have p values between 0.05 and 0.6, with one analysis registering p = 1.03. Hydrogarnets in BW-2 and BW-23 are almost pure hydrogrossular, whereas garnets that nucleate around Cr-spinels in K-1 are solid solutions consisting of uvarovite, grossular, and andradite with minor amounts of schorlomite ($Ca_3(Fe,Ti)_2(Si,Fe)_3O_{12}$) and pyrope (Table 3).

*Diopside*. Diopside occurs as very fine grained, randomly oriented, prismatic or granular crystals that appear to have been in equilibrium with hydrogarnet or garnet. Analyzed crystals have negligible $^{iv}Al$, $Fe^{+3}$, Ti, and Mn, a low $Fe^{+2}/(Fe^{+2}+Mg)$ value (≤ 0.09), and a low $X_{jd}$ (≤ 0.08; Table 4).

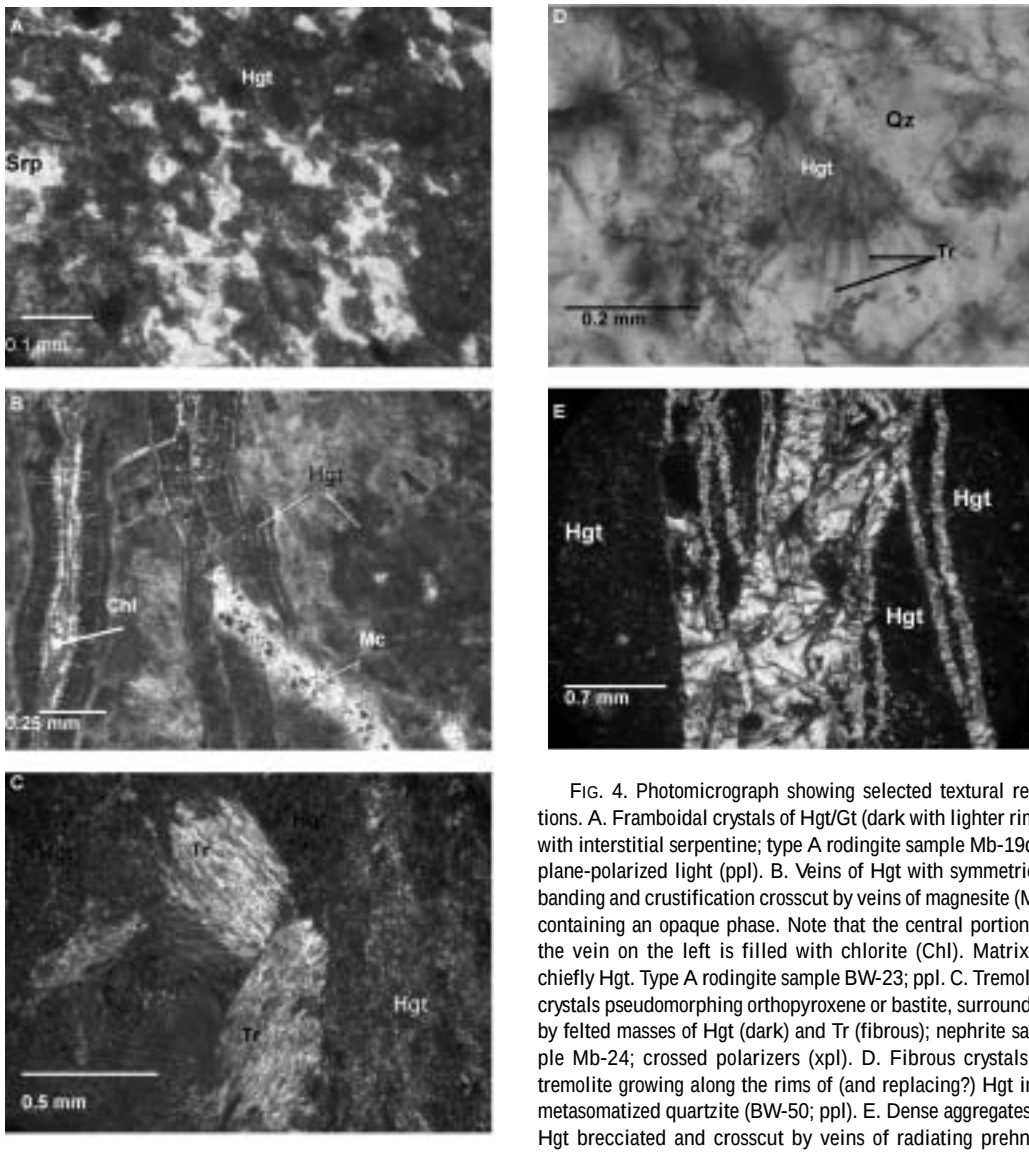


FIG. 4. Photomicrograph showing selected textural relations. A. Framboidal crystals of Hgt/Gt (dark with lighter rims) with interstitial serpentine; type A rodingite sample Mb-19d1; plane-polarized light (ppl). B. Veins of Hgt with symmetrical banding and crustification crosscut by veins of magnesite (Mc) containing an opaque phase. Note that the central portion of the vein on the left is filled with chlorite (Chl). Matrix is chiefly Hgt. Type A rodingite sample BW-23; ppl. C. Tremolite crystals pseudomorphing orthopyroxene or bastite, surrounded by felted masses of Hgt (dark) and Tr (fibrous); nephrite sample Mb-24; crossed polarizers (xpl). D. Fibrous crystals of tremolite growing along the rims of (and replacing?) Hgt in a metasomatized quartzite (BW-50; ppl). E. Dense aggregates of Hgt brecciated and crosscut by veins of radiating prehnite (Prh); type A rodingite sample BW-2 (xpl).

*Tremolite*. Tremolite occurs as very fine grained, fibrous crystals that form dense felted masses with diopside and hydrogarnet, or that define a weak foliation. In type A and B samples, Tr crystallization seems to have continued after the crystallization of Hgt, as evidenced by its occurrence with Prh in veins crosscutting Hgt (e.g., BW-2). In several type C samples (e.g., K-1), the dense aggregates appear to be pseudomorphing an earlier, coarse-grained prismatic mineral (Opx or bastite?; Fig. 4C), and overall become coarser grained toward the outer sheaths of the botryoidal masses. In quartzites, Tr occurs as radiating crystals that commonly replace Hgt (Fig. 4D), and concentrate in fractures and deformed zones. Compositionally, Tr is almost pure with $Fe^{+2}/(Fe^{+2} + Mg) \leq 0.1$, negligible amounts of $Al^{iv}$, and a low A site occupancy (Table 5).

*Pumpellyite*. This mineral occurs as yellowish crystals, less commonly with bluish green rims that form dense masses alternating with Hgt ± Tr–rich zones in some type B blocks (Table 2). In a few samples (e.g. BW-1), Pmp replaces Tr-Act along its rim.

TABLE 3. Representative Analyses of Hgt

| | K-1 | | | | | | | | | | BW-23 | | | | | | BW-2 | |
|---|---|---|---|---|---|---|---|---|---|---|---|---|---|---|---|---|---|---|
| | 21 | 25 | 26 | 28 rim | 33 rim | 34 | 35 | 36 | 40 | 41 rim | 2 | 3 | 5 | 6 | 7 | 17 | 25 | 8 |
| $SiO_2$ | 36.63 | 36.12 | 36.51 | 36.01 | 35.74 | 36.71 | 37.19 | 35.68 | 37.44 | 37.63 | 33.34 | 33.77 | 34.07 | 33.30 | 33.62 | 33.58 | 37.07 | 27.47 |
| $TiO_2$ | 0.70 | 1.25 | 1.06 | 1.41 | 2.54 | 1.40 | 1.15 | 1.13 | 0.74 | 0.86 | – | 0.06 | 0.05 | 0.04 | 0.02 | – | 0.10 | 0.35 |
| $Al_2O_3$ | 6.88 | 7.27 | 8.24 | 6.67 | 5.34 | 6.69 | 7.49 | 5.47 | 7.32 | 6.43 | 23.78 | 24.19 | 24.30 | 23.92 | 23.84 | 23.95 | 23.69 | 22.29 |
| $Cr_2O_3$ | 14.75 | 11.95 | 12.79 | 13.06 | 11.13 | 11.87 | 12.40 | 13.62 | 13.25 | 13.05 | – | – | 0.04 | 0.01 | 0.17 | – | – | 0.01 |
| $Fe_2O_3$ | 5.79 | 6.87 | 6.11 | 6.94 | 8.93 | 7.42 | 6.54 | 7.78 | 6.14 | 6.74 | 0.80 | 0.58 | 0.65 | 0.65 | 0.62 | 0.04 | 0.43 | 0.65 |
| FeO | – | – | – | – | – | – | – | – | – | – | – | – | – | – | – | – | – | – |
| MnO | – | 0.06 | 0.06 | 0.17 | 0.15 | 0.25 | 0.19 | 0.15 | 0.09 | – | 0.07 | 0.07 | – | 0.06 | – | 0.14 | – | 0.10 |
| MgO | 0.41 | 0.12 | 0.09 | 0.54 | 0.35 | 0.19 | 0.17 | 0.16 | 0.51 | 0.62 | – | 0.03 | 0.24 | – | 0.01 | – | 0.21 | 0.11 |
| CaO | 34.18 | 34.99 | 35.84 | 35.20 | 34.64 | 35.27 | 35.56 | 35.07 | 35.29 | 34.29 | 38.44 | 38.03 | 38.96 | 39.17 | 39.14 | 38.35 | 37.26 | 38.78 |
| $H_2O$ | 0.66 | 1.37 | – | 0.00 | 1.18 | 0.20 | – | 0.94 | – | 0.38 | 3.57 | 3.27 | 1.69 | 2.85 | 2.58 | 3.94 | 1.24 | 10.24 |
| Totals1 | 99.34 | 98.63 | 100.70 | 100.00 | 98.82 | 99.80 | 100.69 | 99.06 | 100.78 | 99.62 | 96.43 | 96.73 | 98.31 | 97.15 | 97.42 | 96.06 | 98.76 | 89.76 |
| $Si^{+4}$ | 2.95 | 2.87 | 2.84 | 2.79 | 2.84 | 2.88 | 2.90 | 2.82 | 2.91 | 3.00 | 2.43 | 2.48 | 2.43 | 2.38 | 2.40 | 2.44 | 2.76 | 1.97 |
| H+/4 | 0.09 | 0.18 | 0.00 | 0.00 | 0.16 | 0.03 | 0.00 | 0.12 | 0.00 | 0.05 | 0.43 | 0.40 | 0.20 | 0.34 | 0.31 | 0.48 | 0.16 | 1.23 |
| $Fe^{+3iv}$ | 0.00 | 0.00 | 0.00 | 0.00 | 0.00 | 0.00 | 0.00 | 0.00 | 0.00 | 0.00 | 0.04 | 0.03 | 0.03 | 0.03 | 0.03 | 0.00 | 0.02 | 0.00 |
| $Al^{iv}$ | 0.00 | 0.00 | 0.00 | 0.00 | 0.00 | 0.00 | 0.00 | 0.00 | 0.00 | 0.00 | 0.04 | 0.09 | 0.04 | 0.01 | 0.01 | 0.05 | 0.08 | 0.00 |
| $Ti^{+4}$ | 0.00 | 0.00 | 0.00 | 0.00 | 0.00 | 0.00 | 0.00 | 0.00 | 0.00 | 0.00 | 0.00 | | 0.00 | 0.00 | 0.00 | 0.00 | 0.00 | 0.00 |
| sum tet | 3.04 | 3.05 | 2.84 | 2.79 | 3.00 | 2.91 | 2.90 | 2.94 | 2.91 | 3.05 | 2.94 | 3.00 | 2.70 | 2.76 | 2.75 | 2.97 | 3.02 | 3.20 |
| $Ti^{+4}$ | 0.04 | 0.07 | 0.06 | 0.08 | 0.15 | 0.08 | 0.07 | 0.07 | 0.04 | 0.05 | – | 0.00 | 0.00 | 0.00 | 0.00 | 0.00 | 0.01 | 0.02 |
| $Al^{+3}$ | 0.65 | 0.68 | 0.76 | 0.61 | 0.50 | 0.62 | 0.69 | 0.51 | 0.67 | 0.60 | 2.00 | 2.00 | 2.00 | 2.00 | 2.01 | 2.00 | 2.00 | 1.89 |
| $Cr^{+3}$ | 0.94 | 0.75 | 0.79 | 0.80 | 0.70 | 0.74 | 0.76 | 0.85 | 0.81 | 0.82 | 0.00 | – | 0.00 | 0.00 | 0.01 | 0.00 | 0.00 | 0.00 |
| $Fe^{+3}$ | 0.35 | 0.41 | 0.36 | 0.41 | 0.53 | 0.44 | 0.38 | 0.46 | 0.36 | 0.40 | 0.00 | 0.00 | 0.00 | 0.00 | 0.03 | 0.00 | 0.00 | 0.04 |
| $Mn^{+2}$ | | | | 0.01 | 0.01 | 0.02 | 0.01 | 0.01 | 0.01 | | | | | | | | | 0.01 |
| sum Y | 1.98 | 1.91 | 1.97 | 1.91 | 1.89 | 1.90 | 1.91 | 1.90 | 1.89 | 1.87 | 2.00 | 2.00 | 2.00 | 2.00 | 2.05 | 2.00 | 2.01 | 1.96 |
| $Fe^{+2}$ | – | – | – | – | – | – | – | – | – | – | – | – | – | – | – | – | – | – |
| $Mn^{+2}$ | – | 0.00 | 0.00 | 0.00 | 0.00 | 0.00 | 0.00 | 0.00 | 0.01 | – | 0.00 | 0.00 | 0.00 | 0.00 | 0.00 | 0.01 | 0.00 | 0.00 |
| $Mg^{+2}$ | 0.05 | 0.01 | 0.01 | 0.06 | 0.04 | 0.02 | 0.02 | 0.02 | 0.06 | 0.07 | 0.00 | 0.00 | 0.03 | 0.00 | 0.00 | 0.00 | 0.02 | 0.01 |
| $Ca^{+2}$ | 2.95 | 2.98 | 2.99 | 2.93 | 2.95 | 2.96 | 2.97 | 2.97 | 2.94 | 2.93 | 3.00 | 2.99 | 2.97 | 3.00 | 3.00 | 2.99 | 2.98 | 2.98 |
| sum X | 3.00 | 2.99 | 3.00 | 2.99 | 2.99 | 2.98 | 2.99 | 2.99 | 3.01 | 3.00 | 3.00 | 2.99 | 3.00 | 3.00 | 3.00 | 3.00 | 3.00 | 2.99 |

| | | | | | | | | | | | | | | | | | | | | |
|---|---|---|---|---|---|---|---|---|---|---|---|---|---|---|---|---|---|---|---|---|
| $H^+$ | 0.36 | 0.73 | 0.00 | 0.00 | 0.63 | 0.10 | 0.00 | 0.49 | 0.00 | 0.20 | 1.73 | 1.60 | 0.80 | 1.36 | 1.23 | 1.91 | 0.62 | 4.90 |
| p | 0.05 | 0.13 | 0.16 | 0.21 | 0.16 | 0.12 | 0.10 | 0.18 | 0.09 | 0.00 | 0.57 | 0.52 | 0.57 | 0.62 | 0.60 | 0.56 | 0.24 | 1.03 |
| prp | 0.05 | 0.01 | 0.01 | 0.06 | 0.04 | 0.02 | 0.02 | 0.02 | 0.06 | 0.07 | 0.00 | 0.00 | 0.03 | 0.00 | 0.00 | 0.00 | 0.02 | 0.01 |
| sps | 0.00 | 0.00 | 0.00 | 0.00 | 0.00 | 0.00 | 0.00 | 0.00 | 0.01 | 0.00 | 0.00 | 0.00 | 0.00 | 0.00 | 0.00 | 0.01 | 0.00 | 0.00 |
| uvar | 1.41 | 1.13 | 1.19 | 1.20 | 1.05 | 1.11 | 1.14 | 1.28 | 1.22 | 1.23 | 0.00 | 0.00 | 0.00 | 0.00 | 0.02 | 0.00 | 0.00 | 0.00 |
| schl | 0.06 | 0.11 | 0.09 | 0.12 | 0.23 | 0.12 | 0.11 | 0.11 | 0.06 | 0.08 | 0.00 | 0.00 | 0.00 | 0.00 | 0.00 | 0.00 | 0.02 | 0.03 |
| andr | 0.53 | 0.62 | 0.54 | 0.62 | 0.80 | 0.66 | 0.57 | 0.69 | 0.54 | 0.60 | 0.00 | 0.00 | 0.00 | 0.00 | 0.05 | 0.00 | 0.00 | 0.06 |
| grs | 0.93 | 1.01 | 1.13 | 0.86 | 0.71 | 0.91 | 1.02 | 0.75 | 0.95 | 0.83 | 3.00 | 3.00 | 2.97 | 3.00 | 3.02 | 3.00 | 2.98 | 2.83 |
| | 2.97 | 2.87 | 2.96 | 2.85 | 2.82 | 2.82 | 2.85 | 2.84 | 2.83 | 2.81 | 3.00 | 3.00 | 3.00 | 3.00 | 3.08 | 3.01 | 3.02 | 2.93 |
| Xprp | 0.02 | 0.00 | 0.00 | 0.02 | 0.01 | 0.01 | 0.01 | 0.01 | 0.02 | 0.02 | 0.00 | 0.00 | 0.01 | 0.00 | 0.00 | 0.00 | 0.01 | 0.00 |
| Xsps | 0.00 | 0.00 | 0.00 | 0.00 | 0.00 | 0.00 | 0.00 | 0.00 | 0.00 | 0.00 | 0.00 | 0.00 | 0.00 | 0.00 | 0.00 | 0.00 | 0.00 | 0.00 |
| Xuvar | 0.47 | 0.38 | 0.40 | 0.40 | 0.35 | 0.37 | 0.38 | 0.43 | 0.41 | 0.41 | 0.00 | 0.00 | 0.00 | 0.00 | 0.00 | 0.00 | 0.00 | 0.00 |
| Xschl | 0.02 | 0.04 | 0.03 | 0.04 | 0.08 | 0.04 | 0.04 | 0.04 | 0.02 | 0.03 | 0.00 | 0.00 | 0.00 | 0.00 | 0.00 | 0.00 | 0.01 | 0.01 |
| Xandr | 0.18 | 0.21 | 0.18 | 0.21 | 0.27 | 0.22 | 0.19 | 0.23 | 0.18 | 0.20 | 0.00 | 0.00 | 0.00 | 0.00 | 0.01 | 0.00 | 0.00 | 0.02 |
| Xgrs | 0.31 | 0.34 | 0.38 | 0.29 | 0.24 | 0.30 | 0.34 | 0.25 | 0.32 | 0.28 | 1.00 | 1.00 | 0.99 | 1.00 | 0.98 | 1.00 | 0.99 | 0.94 |

[1]Anhydrous totals

*Chlorite*. Chlorite forms thin linings of Hgt veins in type A rodingites (Fig. 4B), or occurs as a late phase in type B rocks. All chlorites are Mg rich (Mg/Mg + Fe = 0.7 – 0.98) and are classified as clinochlore or sheridanite (Table 6).

*Other phases*. Plagioclase is a minor interstitial phase in type A and B samples. Prehnite (almost pure; Table 5) occurs as radiating crystals along veins that replace or crosscut hydrogarnet in several samples (Fig. 4E). Talc, almost pure with small amounts of Al and $Fe^{+2}$ (Table 6), occurs mixed with serpentine (chrysotile) ± chlorite next to hydrogarnet crystals in a few samples. Spinel occurs in garnet cores or in veins with magnesite or prehnite, and contains appreciable Al but no Ti (Table 6). Carbonates, mostly magnesite, occur in late veins crosscutting veins of prehnite. The predominant species in the serpentinite matrix is chrysotile, with minor amounts of lizardite detected by XRD. Zeolites (natrolite in BW-2 and epistilbite in BW-18a; both identified by XRD) occur in small amounts, and are interpreted as late-stage alteration products of interstitial plagioclase or prehnite.

### *Bulk-rock chemistry*

Bulk-rock major- and trace-element data for several samples representing the different types of metasomatites and some serpentinites of the SMM are listed in Table 7. Data for a metabasaltic sample (BW-44) from a block within the overthrust MMM from the same area are given for comparison. Ignoring CaO and MgO, major-element data for most samples of types A, B, and C metasomatites show that they are all broadly "basaltic," with rather low $K_2O$, $Na_2O$, and $TiO_2$ contents; exceptions include samples BW-1 and Mb-21a, which plot in the trachyandesite and dacite fields of Cox et al. (1979). The data also reveal that type A rodingites tend to have the highest CaO contents, whereas type C nephrites record some of the highest MgO values. On the other hand, type B rodingites exhibit a wide range of MgO and CaO values (Table 7).

Trace-element data are also consistent with type A and B metasomatites having a basaltic protolith, inasmuch as they are characterized by REE abundances in the range of 10–200 times chondritic values (Table 7; Fig. 5). Chondrite-normalized REE patterns reveal that the same samples are LREE enriched, with a weak negative Eu anomaly (Figs. 5A–5D) and a flat HREE pattern. Type C nephrites have the lowest REE concentrations (1–20 times chondrite values) and the most irregular HREE

TABLE 4. Representative Diopside Analyses from K-1[1]

| Analysis # | 3 | 5 | 6 | 7 | 8 | 10 | 12 | 49 | 51 | 52 |
|---|---|---|---|---|---|---|---|---|---|---|
| $SiO_2$ | 54.24 | 53.95 | 54.45 | 54.48 | 54.67 | 54.63 | 54.64 | 54.26 | 54.58 | 55.07 |
| $TiO_2$ | 0.00 | 0.00 | 0.07 | 0.00 | 0.05 | 0.02 | 0.00 | 0.07 | 0.00 | 0.04 |
| $Al_2O_3$ | 1.90 | 1.85 | 1.58 | 1.39 | 1.81 | 1.69 | 2.01 | 1.67 | 1.78 | 0.81 |
| $Cr_2O_3$ | 0.54 | 0.44 | 0.61 | 0.49 | 0.52 | 0.39 | 0.13 | 0.25 | 0.42 | 0.19 |
| $Fe_2O_3$ | 0.28 | 0.47 | 0.91 | 0.36 | 0.27 | 0.92 | 1.77 | 0.00 | 0.00 | 0.00 |
| FeO | 2.61 | 2.56 | 1.94 | 2.89 | 2.60 | 1.84 | 0.97 | 3.17 | 2.71 | 2.95 |
| MnO | 0.13 | 0.14 | 0.13 | 0.30 | 0.04 | 0.13 | 0.07 | 0.19 | 0.02 | 0.16 |
| MgO | 15.23 | 14.73 | 16.14 | 15.19 | 15.40 | 15.78 | 15.84 | 15.50 | 16.02 | 18.31 |
| CaO | 22.23 | 22.86 | 22.16 | 23.20 | 22.90 | 23.09 | 23.04 | 23.73 | 23.74 | 20.30 |
| $Na_2O$ | 1.40 | 1.35 | 1.28 | 1.11 | 1.29 | 1.22 | 1.41 | 1.15 | 1.30 | 0.66 |
| Total | 98.56 | 98.36 | 99.27 | 99.42 | 99.56 | 99.71 | 99.89 | 99.99 | 100.57 | 98.49 |
| $Si^{iv}$ | 2.00 | 2.00 | 1.99 | 2.00 | 1.99 | 1.99 | 1.98 | 1.98 | 1.98 | 2.01 |
| $Al^{iv}$ | 0.00 | 0.00 | 0.01 | 0.00 | 0.01 | 0.01 | 0.02 | 0.02 | 0.02 | 0.00 |
| T site | 2.00 | 2.00 | 2.00 | 2.00 | 2.00 | 2.00 | 2.00 | 2.00 | 2.00 | 2.01 |
| $Al^{vi}$ | 0.08 | 0.08 | 0.06 | 0.06 | 0.07 | 0.06 | 0.07 | 0.05 | 0.05 | 0.04 |
| Ti | 0.00 | 0.00 | 0.00 | 0.00 | 0.00 | 0.00 | 0.00 | 0.00 | 0.00 | 0.00 |
| Cr | 0.02 | 0.01 | 0.02 | 0.01 | 0.01 | 0.01 | 0.00 | 0.01 | 0.01 | 0.01 |
| $Fe^{+3}$ | 0.01 | 0.01 | 0.02 | 0.01 | 0.01 | 0.03 | 0.05 | 0.00 | 0.00 | 0.00 |
| $Fe^{+2}$ | 0.08 | 0.08 | 0.06 | 0.09 | 0.08 | 0.06 | 0.03 | 0.10 | 0.08 | 0.09 |
| $Mn^{+2}$ | 0.00 | 0.00 | 0.00 | 0.01 | 0.00 | 0.00 | 0.00 | 0.01 | 0.00 | 0.00 |
| Mg | 0.84 | 0.81 | 0.88 | 0.83 | 0.84 | 0.86 | 0.86 | 0.84 | 0.86 | 1.00 |
| Ca | 0.88 | 0.91 | 0.87 | 0.91 | 0.89 | 0.90 | 0.89 | 0.93 | 0.92 | 0.79 |
| Na | 0.10 | 0.10 | 0.09 | 0.08 | 0.09 | 0.09 | 0.10 | 0.08 | 0.09 | 0.05 |
| M1,M2 | 2.00 | 2.00 | 2.00 | 2.00 | 2.00 | 2.00 | 2.00 | 2.02 | 2.02 | 1.98 |
| $a_{di}$[2] | 0.84 | 0.81 | 0.88 | 0.83 | 0.84 | 0.86 | 0.86 | 0.84 | 0.86 | 1.00 |
| $a_{jd}$[3] | 0.08 | 0.08 | 0.05 | 0.06 | 0.06 | 0.05 | 0.05 | 0.03 | 0.03 | 0.04 |

[1]Normalized on the basis of 6 equivalent oxygen atoms
[2]Activity calculated as ($X_{Mg}$)
[3]Activity calculated as ($X_{Al}^{vi}$)

patterns (Fig. 5C). The serpentinites are also LREE enriched, but have significantly lower REE concentrations (only 1–30 times chondrite values) and a more irregular pattern that is quite similar to that of type C nephrites (Fig. 5E). On the other hand, sample BW-44 has a flat REE pattern with ~40 times chondrite enrichment in La ($La_N/Ce_N \cong 1.4$; Fig. 5F).

*Microthermometry*

Preliminary microthermometric measurements were carried out on texturally early (isolated or in clusters) fluid inclusions in recrystallized quartz from a quartzite (metachert; BW-39). The host quartz crystals occur in vein-like networks containing stringers of Hgt, radiating needles of Tr, and aggregates of calcite that bind the brecciated chert particles together. All fluid inclusions contain two phases (liquid and vapor), and are characterized by their small sizes (3–13 μm), variable shapes, and constant degrees of fill (usually 5%).

Microthermometric measurements on these inclusions show little if any difference between the isolated variety and those occurring in clusters (Fig. 6). Initial melting temperatures ($Tm_e$) range from –44 to –26°C, with a few inclusions recording values as high as –19.8°C or as low as –56.6°C. Final ice melting temperatures ($Tm_f$) for most inclusions range from –3.4 to 0°C (Fig. 6A). Vapor-to-liquid homogenization temperatures ($T_h$) are more scattered, but generally cluster between 130 and 240°C, with isolated inclusions recording the higher values and greater scatter (Fig. 6B).

TABLE 5. Representative Analyses of Tremolite and Prehnite[1]

| Sample no.: | Tremolite K-1 | | | Prehnite BW-2 | |
|---|---|---|---|---|---|
| | 56 | 59 | 64 | 4 | 22 |
| $SiO_2$ | 56.53 | 57.43 | 57.68 | 43.85 | 43.43 |
| $TiO_2$ | 0.08 | 0.08 | 0.00 | – | – |
| $Al_2O_3$ | 0.30 | 0.43 | 0.41 | 24.68 | 24.47 |
| $Cr_2O_3$ | 0.25 | 0.18 | 0.22 | – | – |
| $Fe_2O_3$ | – | – | – | – | 0.17 |
| FeO | 3.47 | 3.28 | 3.62 | 0.09 | – |
| MnO | 0.02 | 0.16 | 0.00 | 0.00 | 0.04 |
| MgO | 21.66 | 22.25 | 22.39 | – | – |
| CaO | 14.19 | 14.20 | 13.80 | 26.89 | 27.22 |
| $Na_2O$ | 0.32 | 0.41 | 0.35 | – | – |
| $K_2O$ | 0.02 | 0.03 | 0.02 | – | – |
| $H_2O$ | 2.15 | 2.19 | 2.19 | 4.42 | 4.31 |
| Total | 99.00 | 100.62 | 100.67 | 99.93 | 99.65 |
| $Si^{iv}$ | 7.89 | 7.88 | 7.90 | 3.01 | 2.99 |
| $Al^{iv}$ | 0.05 | 0.07 | 0.07 | 0.00 | 0.01 |
| $Ti^{iv}$ | 0.01 | 0.01 | 0.00 | – | – |
| T site | 7.95 | 7.96 | 7.97 | 3.01 | 3.00 |
| $Al^{vi}$ | 0.00 | 0.00 | 0.00 | 2.00 | 1.98 |
| Cr | 0.03 | 0.02 | 0.02 | – | – |
| $Fe^{3+}$ | | | | – | 0.01 |
| Mg | 4.51 | 4.55 | 4.57 | | – |
| $Fe^{+2}$ | 0.41 | 0.38 | 0.40 | 0.01 | – |
| Mn | 0.00 | 0.02 | 0.00 | – | – |
| Ca | 0.06 | 0.03 | 0.00 | – | – |
| M1,2,3 | 5.00 | 5.00 | 5.00 | 2.00 | 1.98 |
| $Fe^{2+}$ | 0.00 | 0.00 | 0.01 | – | – |
| Mn | 0.00 | 0.00 | 0.00 | – | – |
| Ca | 2.00 | 2.00 | 1.99 | – | – |
| Na | 0.00 | 0.00 | 0.00 | – | – |
| M4 | 2.00 | 2.00 | 2.00 | – | – |
| Ca | 0.07 | 0.05 | 0.04 | 1.98 | 2.01 |
| Na | 0.09 | 0.11 | 0.09 | – | – |
| K | 0.00 | 0.01 | 0.00 | – | – |
| Sum A | 0.16 | 0.17 | 0.13 | – | – |
| $a_{tr}$* | 0.57 | 0.59 | 0.60 | 0.99 | 1.00 |

[1]Amphibole formula calculated on the basis of 23 oxygens, tremolite on the basis of 10 O, and Chl on the basis of 14 O.
[2]Activity of Tr = $(X_{Ca})^2*(X_{Mg})^5*(X_{Si})^4$, of Prh = $(X_{Ca})^2.(X_{Si})^3$

## Data Interpretation

### *Protoliths*

Trace elements such as Zr, Nb, and Y, along with the REE are considered relatively immobile over a wide range of conditions; their concentrations are therefore least likely to have been affected by metasomatism (e.g., Meschede, 1986; Grauch, 1989). Discriminant diagrams using these elements are the best tools for identifying protoliths of the metasomatites and their original tectonic settings. The similarity of the chondrite-normalized REE patterns for the variably metasomatized samples presented in this study (Fig. 5) lends credence to the relative

TABLE 6. Representative Analyses of Chlorite, Talc, and Spinel

| | Chlorite BW-23 | | | | Talc BW-2 | Spinel K-1 | | |
|---|---|---|---|---|---|---|---|---|
| | 9 | 10 | 13 | 17 | 15 | 68 | 75 | 76 |
| $SiO_2$ | 27.97 | 29.09 | 28.51 | 27.43 | 61.12 | 0.18 | 0.25 | 0.36 |
| $TiO_2$ | 0.01 | 0.05 | 0.00 | 0.00 | 0.02 | 0.04 | 0.00 | 0.15 |
| $Al_2O_3$ | 24.60 | 22.73 | 21.98 | 25.34 | 1.82 | 21.73 | 27.07 | 25.96 |
| $Cr_2O_3$ | – | – | – | – | 0.06 | 40.84 | 37.93 | 35.85 |
| $Fe_2O_3$ | – | – | – | – | – | 5.09 | 4.90 | 5.84 |
| FeO | 7.61 | 0.65 | 12.82 | 6.87 | 0.07 | 19.21 | 15.92 | 18.96 |
| MnO | 0.21 | 0.00 | 0.13 | 0.12 | 0.15 | 0.48 | 0.55 | 0.45 |
| MgO | 26.75 | 31.69 | 24.67 | 26.37 | 31.31 | 9.83 | 12.84 | 10.71 |
| ZnO | – | – | – | – | – | 0.21 | 0.50 | 0.56 |
| CaO | 0.03 | 0.29 | 0.11 | 0.29 | 0.37 | – | – | – |
| $H_2O$ | 12.54 | 12.93 | 12.24 | 12.58 | | – | – | – |
| Total | 99.71 | 97.44 | 100.47 | 98.99 | 94.92 | 97.61 | 99.96 | 98.84 |
| $Si^{iv}$ | 2.68 | 2.78 | 2.78 | 2.65 | 3.89 | 0.01 | 0.01 | 0.01 |
| $Al^{iv}$ | 1.32 | 1.22 | 1.22 | 1.35 | 0.14 | – | – | – |
| T site | 4.00 | 4.00 | 4.00 | 4.00 | 4.00 | – | – | – |
| $Al^{vi}$ | 1.47 | 1.34 | 1.31 | 1.53 | 0.03 | 0.82 | 0.97 | 0.95 |
| $Cr^{3+}$ | – | – | – | – | 0.00 | 1.04 | 0.91 | 0.88 |
| $Fe^{3+}$ | – | – | – | – | – | 0.12 | 0.11 | 0.14 |
| $Fe^{+2}$ | 0.61 | 0.05 | 1.05 | 0.55 | 0.00 | 0.52 | 0.40 | 0.49 |
| $Mn^{+2}$ | 0.02 | 0.00 | 0.01 | 0.01 | 0.01 | 0.01 | 0.01 | 0.01 |
| Mg | 3.83 | 4.51 | 3.59 | 3.79 | 2.97 | 0.47 | 0.58 | 0.50 |
| $Zn^{2+}$ | – | – | – | – | – | 0.01 | 0.01 | 0.01 |
| Ca | 0.00 | 0.03 | 0.01 | 0.03 | 0.03 | 0.00 | 0.00 | 0.00 |
| $a_{chl}$ | 0.39 | 0.80 | 0.25 | 0.38 | 0.96 | | | |
| $X_{chr}$ | | | | | | 0.52 | 0.46 | 0.44 |
| $X_{mgt}$ | | | | | | 0.12 | 0.11 | 0.14 |
| $X_{hrc}$ | | | | | | 0.35 | 0.39 | 0.45 |

[1]Chlorite formula normalized on the basis of 14 oxygens. Activity formula of clinochlore calculated as {[6/5(XMg)][6(XAliv)]0.2}5; Bryndzia and Scott, 1987.

immobility of these elements (especially the HREE) and justifies their use for petrotectonic interpretations. For type A and B metasomatites, chondrite-normalized REE patterns are very similar to those of ocean-island alkali basalts (BVSP, 1981; Wilson, 1989) or to MORBs affected by metasomatism and LREE enrichment. Relative concentrations of Ti, P, Zr, Nb, and Y also suggest that these rocks were originally ocean-island basalts.

A plot of these concentrations on the Zr–Y–Nb discriminant diagram of Meschede (1986) shows that all samples plot in the field of within-plate alkali basalts or tholeiites (Fig. 7). This conclusion is also supported by the discriminant diagrams of Floyd and Winchester (1975) and the low Zr/Nb (< 10) values. The low Y/Nb (< 1) and La/Yb (< 13) for all samples and the relatively low K/Ba (25–30) ratio for most samples also suggest that these rocks were alkalic (Pearce and Cann, 1973; BVSP, 1981). The only exception is sample BW-18a, which although it plots in the field of "within-plate tholeiites" of Meschede (1986), it has a tholeiitic character similar to that of E-MORBs that also form on oceanic islands.

On the other hand, type C nephrites are extremely depleted in $Al_2O_3$, $Fe_2O_3$*, $TiO_2$, and $P_2O_5$ relative to basalts. Their trace-element concentrations are also significantly different from those of basalts; they have much higher Cr, Ni, and Co, and much lower Nb, Zr, and Y values (Table 7).

## TABLE 7. Bulk-Rock Chemical Composition of Representative Samples

| No.: | BW-2 | BW-18a | BW-23 | Mb-19c | Mb-19d | Mb-19a | Mb-19b | Mb-21a | BW-1 | BW-24 | BW-40 | BW-49 | BW-18b | K-1 | BW-16 | BW-46 | BW-48 | Mb-21b | Mb-21c | BW-11 | BW-12 | BW-22 | BW-47 | BW-14 | BW-44 |
|---|---|---|---|---|---|---|---|---|---|---|---|---|---|---|---|---|---|---|---|---|---|---|---|---|---|
| Type: | A | A | A | A | A | B | B | B/Q | B | B | B | B | B/Srp | C | C | C | C | Q | Q | Serp | Serp | Serp | Serp | CS | Basalt |
| $SiO_2$ | 39.51 | 46.52 | 33.34 | 41.62 | 35.18 | 46.55 | 40.85 | 64.30 | 60.48 | 47.30 | 49.56 | 52.41 | 39.79 | 53.75 | 56.53 | 56.85 | 56.82 | 87.00 | 92.28 | 37.82 | 33.82 | 36.41 | 37.44 | 22.87 | 48.18 |
| $TiO_2$ | 1.00 | 0.31 | <0.01 | 0.89 | 1.40 | 0.90 | 0.77 | 0.92 | 0.97 | 0.08 | 0.18 | 0.30 | 0.15 | 0.02 | <0.01 | <0.01 | 0.01 | 0.33 | 0.22 | <0.01 | <0.01 | 0.04 | <0.01 | <0.01 | 1.74 |
| $Al_2O_3$ | 11.82 | 5.00 | 21.23 | 15.09 | 13.77 | 19.23 | 20.35 | 13.03 | 14.64 | 2.26 | 4.91 | 4.31 | 4.55 | 0.91 | 0.61 | 0.39 | 0.26 | 4.91 | 3.43 | 0.79 | 0.93 | 2.41 | 1.00 | 0.87 | 14.40 |
| $Fe_2O_3$ | 6.39 | 3.39 | 0.45 | 6.26 | 11.01 | 7.12 | 6.23 | 7.06 | 7.01 | 5.10 | 5.50 | 5.31 | 5.25 | 4.45 | 5.04 | 5.02 | 5.20 | 1.94 | 0.71 | 6.65 | 18.80 | 7.15 | 13.11 | 4.76 | 14.19 |
| MnO | 0.11 | 1.02 | 0.07 | 0.21 | 0.56 | 0.10 | 0.11 | 0.16 | 0.06 | 0.20 | 0.31 | 0.29 | 0.40 | 0.19 | 0.25 | 0.13 | 0.16 | 0.06 | 0.04 | 0.08 | 0.09 | 0.14 | 0.15 | 0.15 | 0.18 |
| MgO | 13.82 | 8.65 | 8.96 | 1.75 | 9.52 | 2.23 | 2.07 | 2.45 | 2.01 | 19.99 | 24.32 | 18.04 | 33.67 | 18.22 | 21.84 | 21.91 | 21.30 | 0.80 | 0.29 | 36.34 | 33.05 | 32.39 | 34.30 | 18.39 | 8.68 |
| CaO | 15.87 | 30.04 | 26.57 | 30.39 | 22.67 | 16.39 | 22.81 | 3.55 | 5.07 | 19.80 | 8.30 | 14.15 | 0.57 | 18.56 | 12.54 | 13.01 | 13.49 | 1.12 | 0.49 | 1.94 | 0.38 | 4.93 | 0.25 | 19.23 | 2.34 |
| $Na_2O$ | 0.14 | 0.29 | 0.10 | 0.92 | 0.21 | 3.25 | 1.20 | 7.56 | 8.06 | 0.15 | 0.33 | 0.45 | 0.46 | 0.59 | 0.24 | 0.21 | 0.20 | 2.90 | 2.06 | 0.23 | 0.19 | 0.20 | 0.22 | 0.21 | 1.43 |
| $K_2O$ | 0.12 | 0.06 | 0.04 | 0.05 | 0.03 | 0.08 | 0.05 | 0.14 | 0.25 | 0.03 | 0.05 | 0.06 | 0.04 | 0.05 | 0.04 | 0.05 | 0.05 | 0.09 | 0.05 | 0.03 | 0.03 | 0.04 | 0.06 | 0.05 | 2.16 |
| $P_2O_5$ | 0.07 | 0.05 | 0.01 | 0.09 | 0.16 | 0.05 | 0.07 | 0.12 | 0.12 | <0.01 | 0.07 | 0.10 | 0.07 | 0.01 | <0.01 | <0.01 | 0.01 | 0.06 | 0.06 | 0.01 | 0.01 | 0.01 | <0.01 | <0.01 | 0.21 |
| LOI | 10.24 | 4.26 | 8.12 | 1.62 | 5.04 | 3.41 | 4.45 | 0.51 | 0.78 | 2.89 | 6.38 | 4.25 | 14.69 | 1.85 | 2.64 | 2.35 | 2.19 | 0.53 | 0.27 | 15.50 | 11.76 | 15.54 | 12.83 | 28.01 | 6.11 |
| Totals | 99.13 | 99.60 | 98.89 | 98.94 | 99.62 | 99.39 | 99.02 | 99.83 | 99.57 | 98.43 | 99.92 | 99.68 | 99.65 | 98.84 | 99.80 | 99.99 | 99.71 | 99.76 | 99.90 | 99.68 | 99.43 | 99.65 | 99.71 | 94.97 | 99.68 |
| | | | | | | | | | | | | | ppm | | | | | | | | | | | | |
| Cr | 100 | 30 | 10 | 90 | 340 | 80 | 80 | 60 | 100 | 4030 | 30 | 30 | 40 | 1210 | 490 | 440 | 120 | 30 | 50 | 2010 | 2120 | 1960 | 2060 | 1770 | 90 |
| Ni | 55 | 30 | 15 | 40 | 215 | 45 | 40 | 40 | 55 | 565 | 30 | 40 | 35 | 930 | 415 | 705 | 190 | 20 | 10 | 1510 | 1835 | 560 | 1690 | 1545 | 55 |
| Co | 20.5 | 9 | 1.5 | 24 | 61.5 | 25 | 22.5 | 13.5 | 20 | 48.5 | 17 | 17.5 | 61 | 50 | 39.5 | 62.5 | 31.5 | 22 | 3 | 92 | 155 | 55.5 | 112 | 97 | 55 |
| V | 125 | 50 | 10 | 115 | 205 | 105 | 90 | 75 | 120 | 150 | 20 | 30 | 55 | 15 | 10 | 5 | 5 | 35 | 10 | 30 | 50 | 105 | 50 | 25 | 340 |
| Rb | 5.4 | 11.6 | 11.4 | 9.8 | 13 | 9 | 8.8 | 15.2 | 10.6 | 10.2 | 14.6 | 11.8 | 19 | 11 | 11.2 | 11 | 9.2 | 13.6 | 5.2 | 10.8 | 11.2 | 10.2 | 13.4 | 10.2 | 102 |
| Cs | 0.4 | 0.5 | 0.1 | 0.1 | 0.1 | <0.1 | <0.1 | 0.9 | 0.4 | 0.1 | 0.2 | 0.1 | 1.6 | 0.1 | <0.1 | <0.1 | <0.1 | 0.4 | <0.1 | <0.1 | <0.1 | 0.1 | 0.1 | 0.1 | 1.8 |
| Sr | 258 | 65.3 | 38.9 | 364 | 116.5 | 469 | 425 | 113.5 | 936 | 20.9 | 123.5 | 127 | 73.9 | 28.8 | 46.8 | 27.9 | 40 | 43.5 | 25.2 | 120 | 10.5 | 86.7 | 54.1 | 1415 | 61.5 |
| Ba | 44.5 | 6.5 | 16 | 22.5 | 23 | 29.5 | 18 | 41.5 | 200 | 14.5 | 17.5 | 12 | 6 | 17 | 48 | 3.5 | 12 | 22 | 10.5 | 8.5 | 14 | 9.5 | 9.5 | 14 | 183 |
| Nb | 24 | 18 | 13 | 29 | 35 | 26 | 24 | 26 | 24 | 10 | 19 | 16 | 23 | 8 | 9 | 9 | 6 | 19 | 12 | 13 | 10 | 11 | 10 | 13 | 23 |
| Zr | 331 | 109 | 46.5 | 187 | 289 | 159.5 | 143 | 152.5 | 216 | 25 | 108.5 | 108.5 | 140 | 28 | 40.5 | 24.5 | 21 | 90 | 43 | 44.5 | 35.5 | 19.5 | 21.5 | 42 | 176.5 |
| Y | 28.5 | 17.5 | 7.5 | 25.5 | 39.5 | 22.5 | 22 | 26 | 31.5 | 8.5 | 15 | 18.5 | 22.5 | 3.5 | 5 | 4 | 3 | 14 | 9.5 | 5.5 | 5 | 6 | 3.5 | 8 | 50 |
| Hf | 8 | 3 | 1 | 4 | 7 | 4 | 3 | 4 | 5 | <1 | 4 | 2 | 4 | <1 | 1 | <1 | <1 | 3 | <1 | 1 | <1 | <1 | <1 | 1 | 5 |
| Cu | 120 | 5 | <5 | 10 | 25 | 20 | 25 | 50 | 30 | 250 | 15 | 10 | 15 | <5 | <5 | <5 | 10 | 35 | 55 | 5 | 30 | 120 | 5 | 10 | 40 |
| Mo | 10 | 8 | 6 | 8 | 6 | 6 | 6 | 6 | 8 | 6 | 10 | 6 | 8 | 8 | 8 | 8 | 6 | 8 | 6 | 8 | 8 | 6 | 6 | 8 | 8 |
| Zn | 95 | 65 | 15 | 70 | 70 | 85 | 105 | 70 | 95 | 35 | 60 | 70 | 60 | 100 | 40 | 30 | 25 | 35 | 15 | 50 | 35 | 25 | 65 | 40 | 160 |
| Pb | 20 | <5 | <5 | 15 | 5 | 15 | 15 | 5 | 15 | <5 | 5 | <5 | <5 | <5 | <5 | <5 | <5 | 5 | 5 | <5 | <5 | 5 | <5 | 5 | 10 |
| Sn | 9 | 6 | 7 | 8 | 9 | 9 | 7 | 7 | 9 | 6 | 9 | 6 | 8 | 5 | 7 | 6 | 5 | 6 | 5 | 5 | 5 | 5 | 6 | 7 | 8 |
| W | 5 | 15 | 4 | 69 | 16 | 71 | 66 | 4 | 4 | 3 | 3 | 5 | 5 | 5 | 3 | 5 | 3 | 149 | 3 | 4 | 7 | 4 | 7 | 3 | 6 |
| La | 27.5 | 17 | 3.5 | 32.5 | 43.5 | 32.5 | 33.5 | 26.5 | 30 | 3.5 | 7.5 | 13.5 | 17.5 | 3 | 4 | 2.5 | 3.5 | 10.5 | 7.5 | 4 | 5.5 | 2.5 | 3.5 | 13.5 | 11.5 |
| Ce | 59.5 | 37 | 2.5 | 65.5 | 91.5 | 65.5 | 67 | 68.5 | 56.5 | 2.5 | 20 | 37 | 40 | 2.5 | 3.5 | 2 | 3 | 24.5 | 17.5 | 3 | 7 | 1.5 | 2.5 | 8.5 | 21 |
| Pr | 6.2 | 3.6 | 0.3 | 7.3 | 10.2 | 7.2 | 7.4 | 6.2 | 6.7 | 0.3 | 2 | 3.2 | 4.2 | 0.3 | 0.4 | 0.1 | 0.4 | 2.3 | 1.7 | 0.3 | 0.9 | 0.1 | 0.3 | 1.5 | 3.1 |
| Nd | 23.5 | 13 | 1 | 27.5 | 37.5 | 26 | 27 | 23 | 26.5 | 0.5 | 8.5 | 12 | 16 | 0.5 | 1 | 0.5 | 1 | 8.5 | 6.5 | 1 | 3 | 0.5 | 1 | 5 | 14.5 |
| Sm | 4.6 | 2.5 | 0.2 | 5.3 | 7.8 | 5 | 5.2 | 4.6 | 5.2 | 0.3 | 2.3 | 2.5 | 3.3 | 0.1 | 0.1 | 0.1 | 0.2 | 1.7 | 1.4 | 0.2 | 0.5 | 0.3 | 0.1 | 0.6 | 5.1 |
| Eu | 0.9 | 0.5 | <0.1 | 1.1 | 1.7 | 1.1 | 1 | 1.1 | 1.2 | 0.1 | 0.4 | 0.6 | 0.1 | 0.1 | <0.1 | <0.1 | <0.1 | 0.3 | 0.3 | <0.1 | 0.1 | <0.1 | <0.1 | 0.2 | 1.8 |
| Gd | 4.2 | 2.4 | 0.3 | 5.2 | 7.8 | 4.8 | 5.1 | 4.7 | 5 | 0.4 | 2.2 | 3.2 | 3 | 0.2 | 0.1 | 0.2 | 0.3 | 1.9 | 1.3 | 0.2 | 0.5 | 0.5 | 0.1 | 0.7 | 6.6 |
| Tb | 0.7 | 0.4 | 0.1 | 0.7 | 1.2 | 0.7 | 0.7 | 0.8 | 0.8 | 0.1 | 0.4 | 0.5 | 0.5 | <0.1 | <0.1 | <0.1 | <0.1 | 0.3 | 0.2 | <0.1 | <0.1 | 0.1 | <0.1 | 0.1 | 1.3 |
| Dy | 4.5 | 2.8 | 1 | 4.5 | 6.9 | 4.1 | 4 | 4.2 | 5 | 1.2 | 2.5 | 3.1 | 3.5 | 0.5 | 0.7 | 0.5 | 0.4 | 2.1 | 1.5 | 0.7 | 0.7 | 1 | 0.5 | 1 | 8.4 |
| Ho | 1 | 0.6 | 0.3 | 0.9 | 1.4 | 0.9 | 0.9 | 0.9 | 1.1 | 0.3 | 0.6 | 0.6 | 0.8 | 0.1 | 0.1 | 0.1 | 0.1 | 0.5 | 0.3 | 0.2 | 0.1 | 0.2 | 0.1 | 0.3 | 1.9 |
| Er | 3.2 | 2.1 | 1.1 | 2.9 | 4.4 | 2.7 | 2.5 | 2.8 | 3.6 | 1 | 1.7 | 2.1 | 2.7 | 0.5 | 0.8 | 0.6 | 0.4 | 1.6 | 1.1 | 0.9 | 0.7 | 0.8 | 0.5 | 1.1 | 5.5 |
| Tm | 0.5 | 0.3 | 0.1 | 0.4 | 0.7 | 0.4 | 0.3 | 0.4 | 0.6 | 0.1 | 0.3 | 0.3 | 0.4 | <0.1 | 0.1 | <0.1 | 0.1 | 0.3 | 0.1 | 0.1 | 0.1 | 0.1 | <0.1 | 0.1 | 0.9 |
| Yb | 3.5 | 2.2 | 1.5 | 3 | 5 | 2.9 | 2.6 | 2.9 | 3.9 | 1.1 | 2.2 | 2.3 | 3.1 | 0.7 | 1.2 | 0.7 | 0.6 | 2 | 1.1 | 1.1 | 0.8 | 0.8 | 0.6 | 1.4 | 5.7 |
| Lu | 0.5 | 0.3 | 0.2 | 0.4 | 0.7 | 0.4 | 0.4 | 0.4 | 0.6 | 0.1 | 0.3 | 0.3 | 0.5 | 0.1 | 0.1 | <0.1 | <0.1 | 0.3 | 0.1 | 0.1 | 0.1 | 0.1 | <0.1 | 0.2 | 0.8 |
| Ga | 4 | 3 | 6 | 9 | 7 | 16 | 18 | 15 | 17 | 3 | 7 | 4 | 3 | 3 | 2 | 1 | 1 | 6 | 4 | 3 | 3 | 2 | 1 | 5 | 23 |
| Ta | 1.5 | 1.5 | 1 | 5 | 3 | 5.5 | 5 | 2 | 1.5 | 0.5 | 1.5 | 1.5 | 2 | 0.5 | 0.5 | 0.5 | <0.5 | 6.5 | 0.5 | 1.5 | 0.5 | 0.5 | 0.5 | 1 | 2 |
| Th | 11 | 8 | 4 | 12 | 14 | 11 | 13 | 10 | 10 | 3 | 6 | 6 | 11 | 1 | 2 | 1 | <1 | 4 | 3 | 3 | 1 | <1 | 1 | 4 | 3 |
| U | 2.5 | 1 | 0.5 | 1.5 | 2.5 | 1.5 | 1.5 | 1 | 1.5 | <0.5 | 1 | 1.5 | 1.5 | <0.5 | <0.5 | <0.5 | <0.5 | 0.5 | 0.5 | 0.5 | 0.5 | 0.5 | 0.5 | 0.5 | 0.5 |

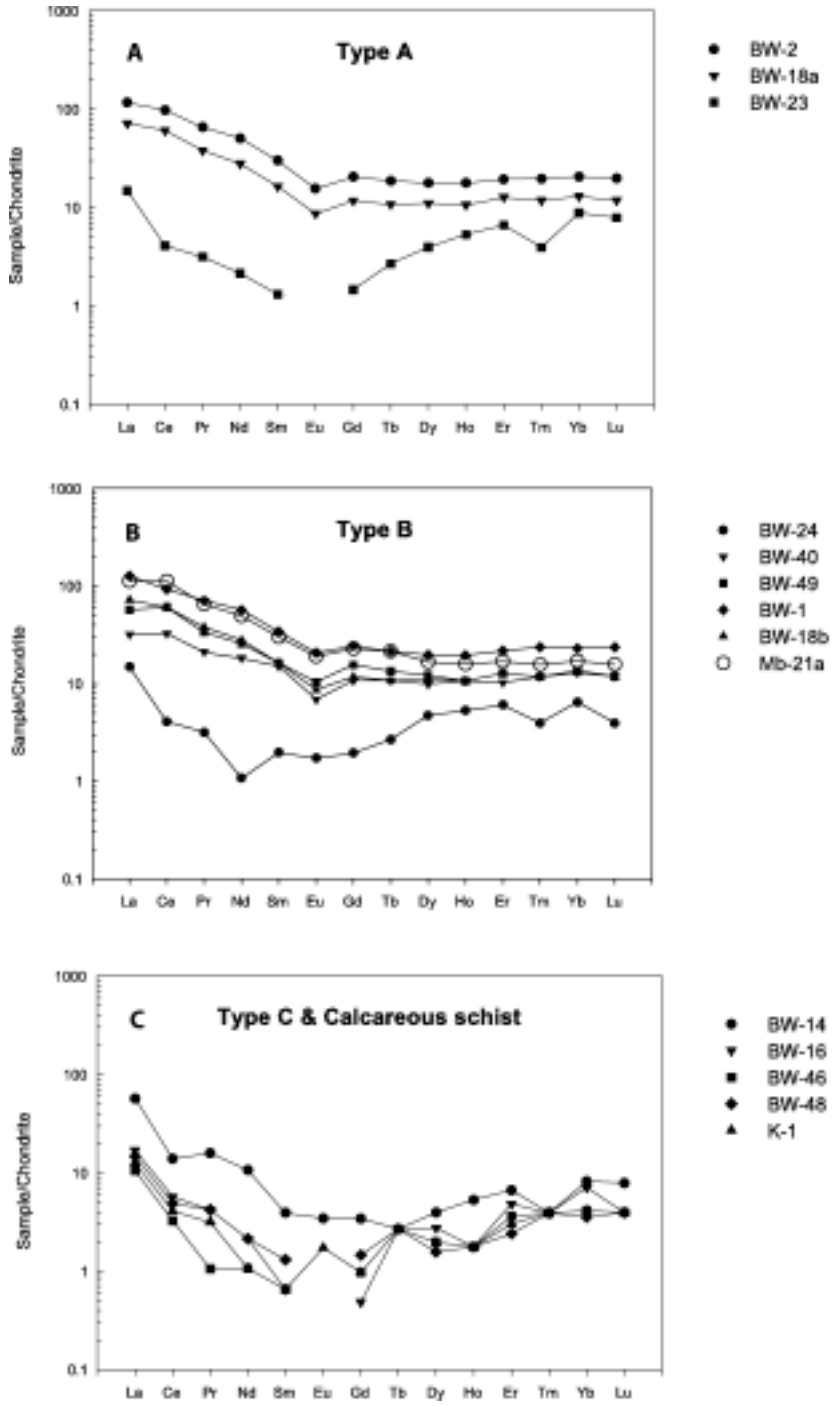


FIG. 5. Chondrite-normalized rare-earth-element diagrams for (A) Type A rodingites, (B) type B metasomatites, (C) Type C nephrites and calcareous schist sample BW-14, (D) sample Mb-19 a–d, (E) serpentinites, and (F) sample BW-44, an unmetasomatized metabasalt from the MMM.

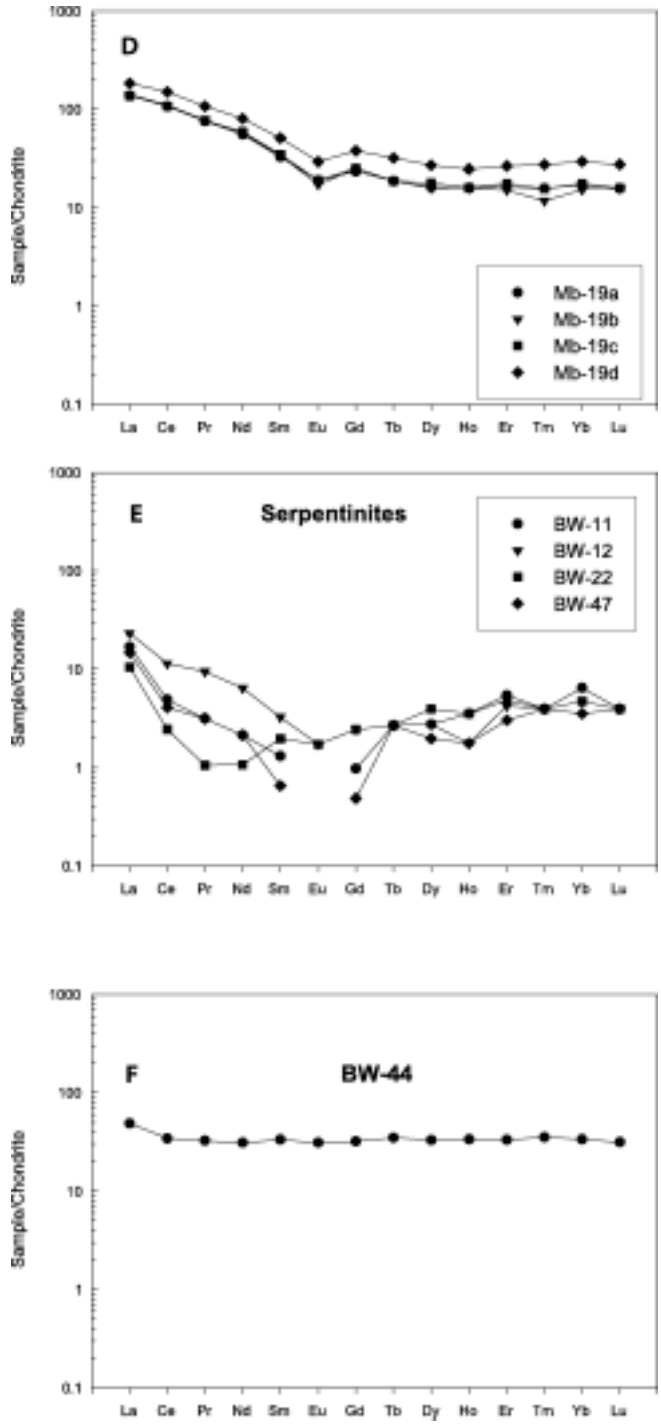


Fig. 5 *Continued*

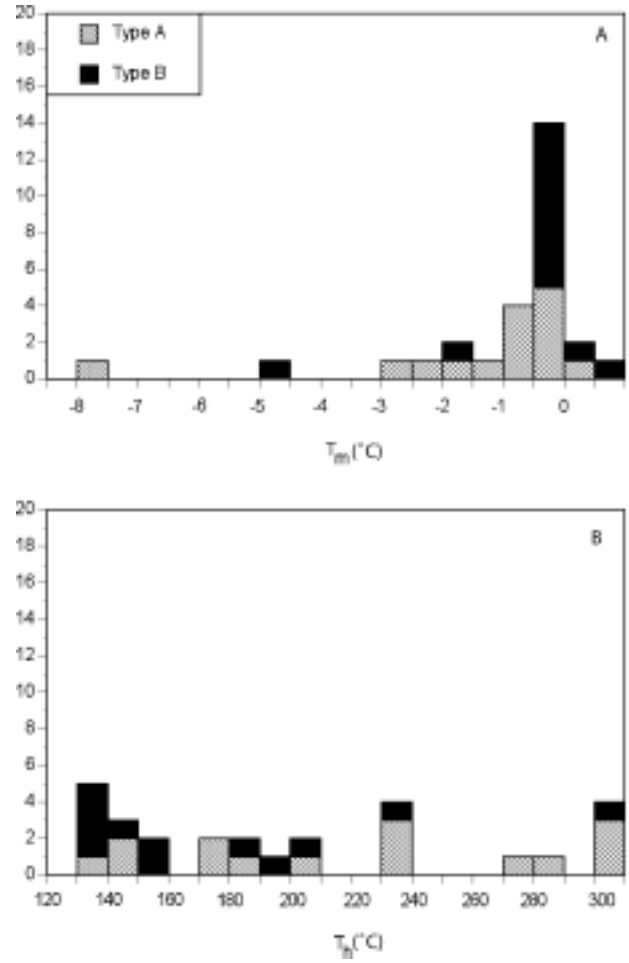


FIG. 6. Histograms for temperatures of (A) final melting of ice ($Tm_f$) and (B) homogenization ($T_h$; vapor to liquid), for texturally early (isolated or in clusters) fluid inclusions in quartz from a metasomatized quartzite (BW-39).

Their REE concentrations are also lower than most type A and B metasomatites (only 20 times or less chondritic values); their patterns are much more irregular and very similar to serpentinites (Fig. 5C). Because some of these samples define reaction zones between quartzites and serpentinites (e.g. BW-48), we conclude that type C nephrites represent metasomatized peridotites/serpentinites. This conclusion is supported by the pseudomorphic replacement textures, and is similar to the conclusions of Capedri et al. (1978), Wares and Martin (1980), Prokhor (1991), O'Hanley (1996), and Harlow and Sorensen (2004) who all report the metasomatism of serpentinites to form nephrites.

These conclusions are consistent with field relations and the tectonic setting of the study area. El-Shazly et al. (1994) reported several tectonic blocks of ocean alkali basalts within the mélange of Ruwi, now metamorphosed under pumpellyite-actinolite to lawsonite-albite facies conditions. The same mélange contains blocks or lenses of marbles and quartzites. Moreover, the muddy matrix mélange that structurally overlies the SMM in the study area also contains blocks of unmetasomatized basalts, along with marbles and quartzites. Sample BW-44, which represents one of these unmetasomatized basaltic blocks from the MMM, has a composition typical of P-MORB (E-MORB) type basalts, as

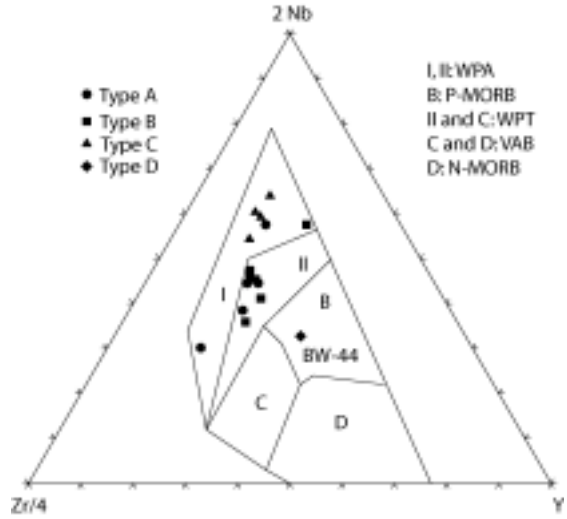


FIG. 7. Plots of metasomatic rocks from the SMM of Bawshir and Al-Khuwair on the trace-element discriminant diagram of Meschede (1986). Abbreviations: WPA = within-plate alkali basalts; P-MORB = primitive mid-ocean ridge basalt; WPT = within-plate tholeiite, VAB = volcanic-arc basalt; N-MORB = normal mid-oceanic ridge basalt.

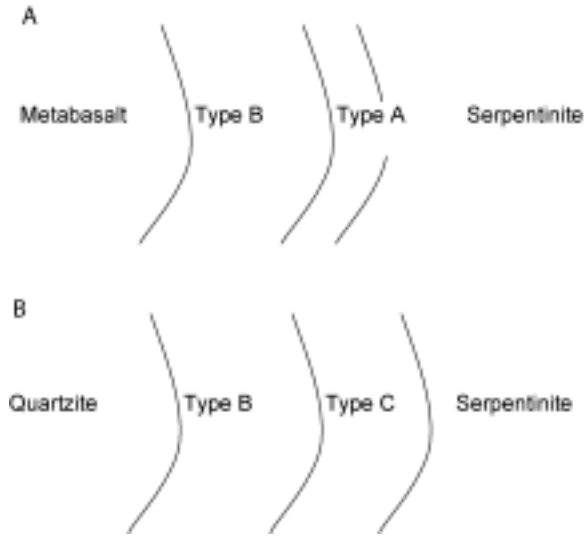


FIG. 8. Schematic diagram showing the "reaction fronts" commonly developed around (A) the metabasaltic blocks in the SMM and (B) the quartzite blocks in the SMM. Both diagrams are not drawn to scale.

indicated by its REE pattern (Fig. 5F) and various discriminant diagrams (Fig. 7). It is therefore reasonable to conclude that similar basaltic blocks were caught in the underthrust serpentinite matrix mélange.

*Chemical changes and element mobility during metasomatism*

In the study area, metasomatic fronts developed between serpentinites and enclosed basaltic (or metabasaltic) blocks on one hand, and cherts (or

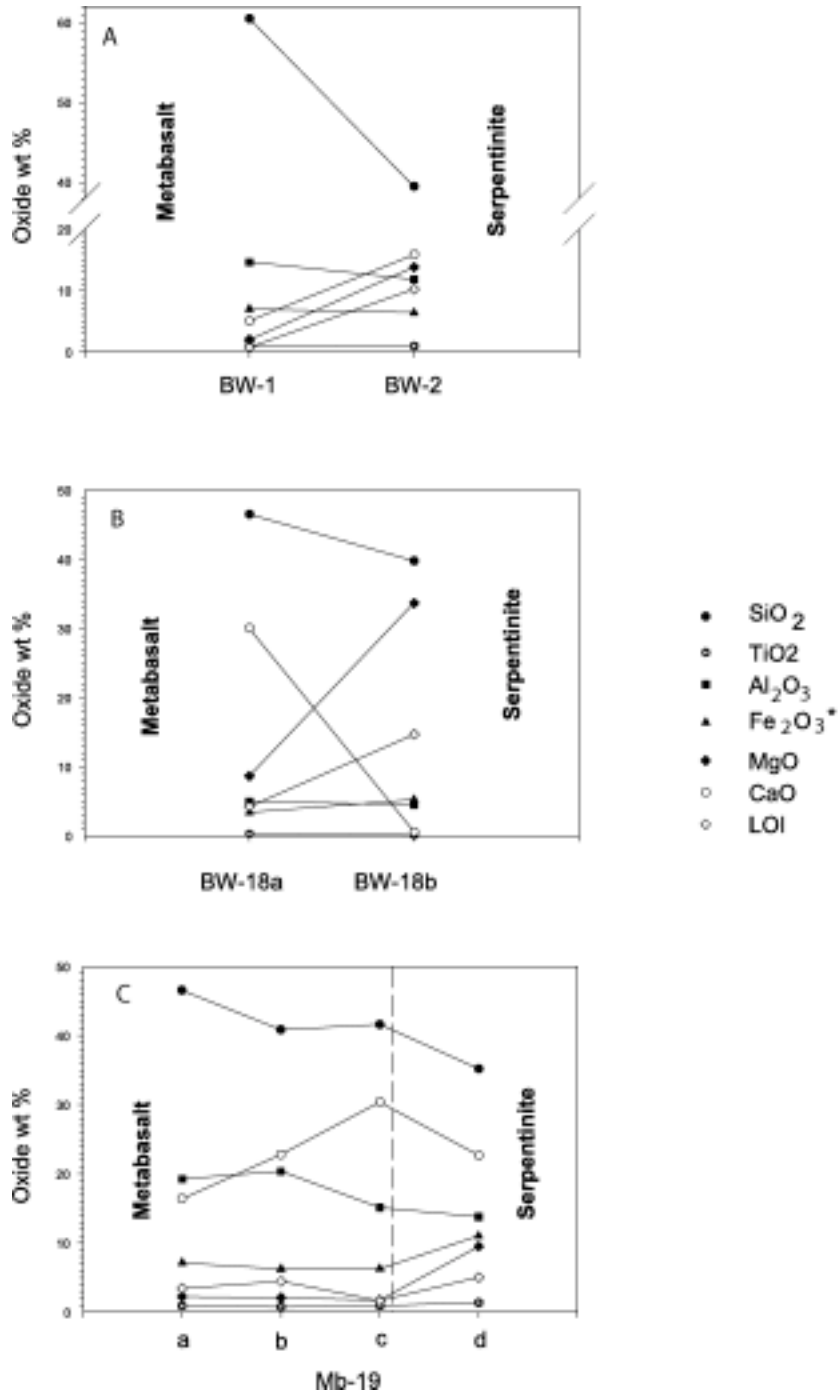


FIG. 9. Schematic plots of major-element compositional profiles across different metasomatic zones between serpentinites and their enclosed metabasalts (A–C), and quartzites (D–E). Vertical dashed line on Figures C–E represent the relative locations of the original boundaries between the serpentine and the enclosed block, as surmised from the abrupt change in the concentration of $Al_2O_3$, taking into account the location of type C nephrites (which formed after the serpentinites).

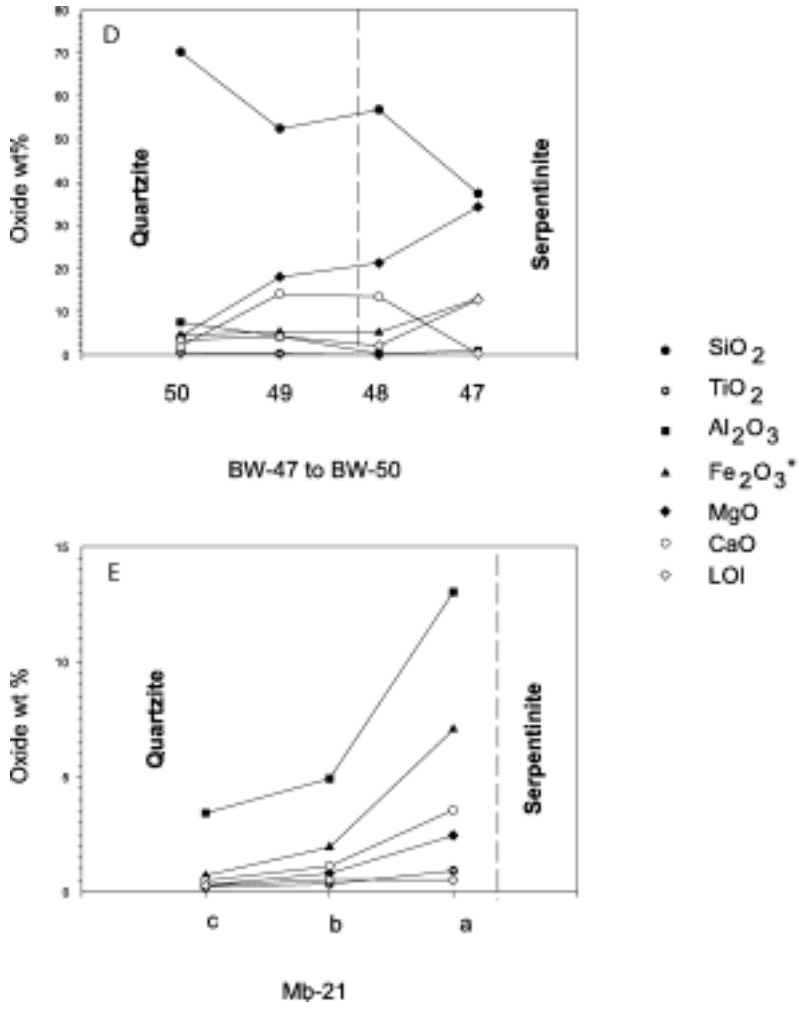


FIG. 9. *Continued*

quartzites) on the other. Unfortunately, extensive quarrying for marble blocks in this area have destroyed many of the original field relations, leaving behind many tectonic blocks as float or tailings, and only a few blocks remain embedded in the serpentinites with well-developed reaction fronts. Where such fronts and reaction zones are preserved, metabasaltic blocks are typically separated from the serpentinites first by a zone of type B metasomatites, followed by a zone of type A rodingites (Fig. 8A). The quartzite blocks are separated from their host serpentinites first by type B metasomatites followed by a zone of type C nephrites (Fig. 8B).

Major-element profiles across the metasomatic zones between metabasalts and serpentinites reveal that whereas CaO and MgO increase toward the serpentinite, $SiO_2$ and alkalis decrease significantly. $Al_2O_3$, $Fe_2O_3$*, and $TiO_2$ remain more or less unchanged (Figs. 9A–9C). Profiles between the serpentinites and the enclosed quartzite blocks exhibit a more or less similar pattern, except for $Al_2O_3$ and $Fe_2O_3$*, which increase toward the serpentinite (Figs. 9D and 9E) and alkalis that either decrease or increase in the same direction. Assuming that $Al_2O_3$ was relatively immobile during metasomatism, the sharp change in the

concentration of $Al_2O_3$ probably represents the original boundary between the block and the enclosing serpentinite (dashed line on Figs. 9C, 9D, and 9E; Brady, 1977; Sanford, 1982). For most samples, this boundary also marks a sharp change in the concentrations of Cr and Zr, which are also considered relatively immobile (e.g., Sanford, 1982; Meschede, 1986).

Understanding the process of Ca-metasomatism in the Bawshir–Al-Khuwair area requires identifying the changes that have affected the protoliths of these rocks, as illuminated using isocon diagrams (Grant, 1986). Assuming that all type A and B blocks were originally oceanic basalts, most of which formed on islands (OIBs), isocon diagrams were constructed using Sun and McDonough's (1989) data for Gough Island (analysis G111) as a representative of their OIB protolith for all elements except for Cr, Ni, and V. OIB values for Cr and Ni were taken as the "crude median" estimates from Prinz's (1967) data. The V concentration in OIB was estimated at 177 ppm assuming a Ti/V ratio of 100 (Shervais, 1982). For sample BW-18a which has a tholeiitic character, major- and trace-element data were plotted against average E-MORB values from Staudigel et al. (1996) and Sun and McDonough (1989). E-MORB Values for Cr, Ni, and V (not provided by these data bases) were estimated at 442, 205, and 250 ppm, respectively, using the algorithms of Miyashiro and Shido (1975). All results are plotted on Figures 10 through 15.

On major- and trace-element isocon diagrams, no group of elements defines a straight line passing through the origin for any of type A or B samples (Figs. 10–15). This indicates that even relatively immobile elements as Al, Ti, Zr, and Nb were "decoupled" during metasomatism. If it is assumed that metasomatism occurred with no change in mass, major-element isocon diagrams show that all type A rodingites formed from their basaltic protolith by gaining CaO and volatiles, and losing $SiO_2$, $Fe_2O_3$*, alkalis, $P_2O_5$, $TiO_2$, and in most cases, $Al_2O_3$ (Fig. 10). Similar changes would also be required for the formation of type B metasomatites from basaltic protoliths without a change in mass, although this would require the loss of larger amounts of $Al_2O_3$ and the addition of MgO in some cases (Fig. 11).

It is unlikely that Ca-metasomatism took place with no change in mass, particularly because it was associated with an increase in density. Assuming a density of 2.9 g/cm$^3$ for the basaltic protolith, the formation of type A rodingites (65% Gt, 35% Di by volume yielding a density of ~ 3.5 g/cm$^3$) and type B metasomatites (30% Gt, 40% Di, and 30% Tr for a density of ~3.3 g/cm$^3$) would require a density increase of ~21% and 14%, respectively. Constant mass and increasing density would necessitate an equivalent decrease in volume, for which there is no evidence. On the other hand, the common occurrence of metamorphic replacement textures, particularly in type B and C blocks, suggests that metasomatism was accompanied by no (or little) change in volume, a conclusion similar to that arrived at by Coleman (1967) and Schandl et al. (1989) for other rodingites. Assuming that Ca-metasomatism in Bawshir was largely isovolumetric, the formation of type A rodingites from their basaltic protoliths (represented by the dashed lines on Figs. 10 and 13) would require the addition of CaO and volatiles, the loss of alkalis, $SiO_2$, $Al_2O_3$, $Fe_2O_3$*, P, Ti, Nb, Sr, Ba, Rb, Cr, Ni, and V, and little change in the concentrations of Zr and Y. MgO was either lost or remained more or less unchanged during metasomatism. Similarly, the formation of type B metasomatites would require the addition of CaO, volatiles ± MgO, and the loss of variable amounts of all other elements (Figs. 11 and 14). The elements that appear to have been least affected by metasomatism are Y, Zr, and in some cases Nb, Al, and Si. On the other hand, the formation of type C nephrites at the expense of the serpentinites must have involved the addition of CaO, $SiO_2$, Cr, Zr, Nb, and volatiles, along with smaller amounts of $Fe_2O_3$*, $Al_2O_3$, and leaching of some MgO (Figs. 12 and 15). Metasomatism of the quartzites (if isovolumetric) must have involved the loss of $SiO_2$ and the gain of CaO and MgO.

The analysis of the major- and trace-element data presented above leads to the conclusion that the metasomatic rocks formed by the introduction of $Ca^{2+}$ into the basaltic and quartzitic blocks, and the removal of $SiO_2$ and/or alkalis, indicating a bimetasomatic process (e.g., Frantz and Mao, 1979). Because the reaction fronts are only several centimeters to decimeters thick, diffusion must have been the primary mechanism for metasomatism, although infiltration must have played a significant (or even dominant) role in metasomatizing some fractured quartzites and in forming the late-stage veins of type A rinds. In such cases, the infiltrating fluid must have been derived from the serpentinites, as indicated by the observed decrease in the number

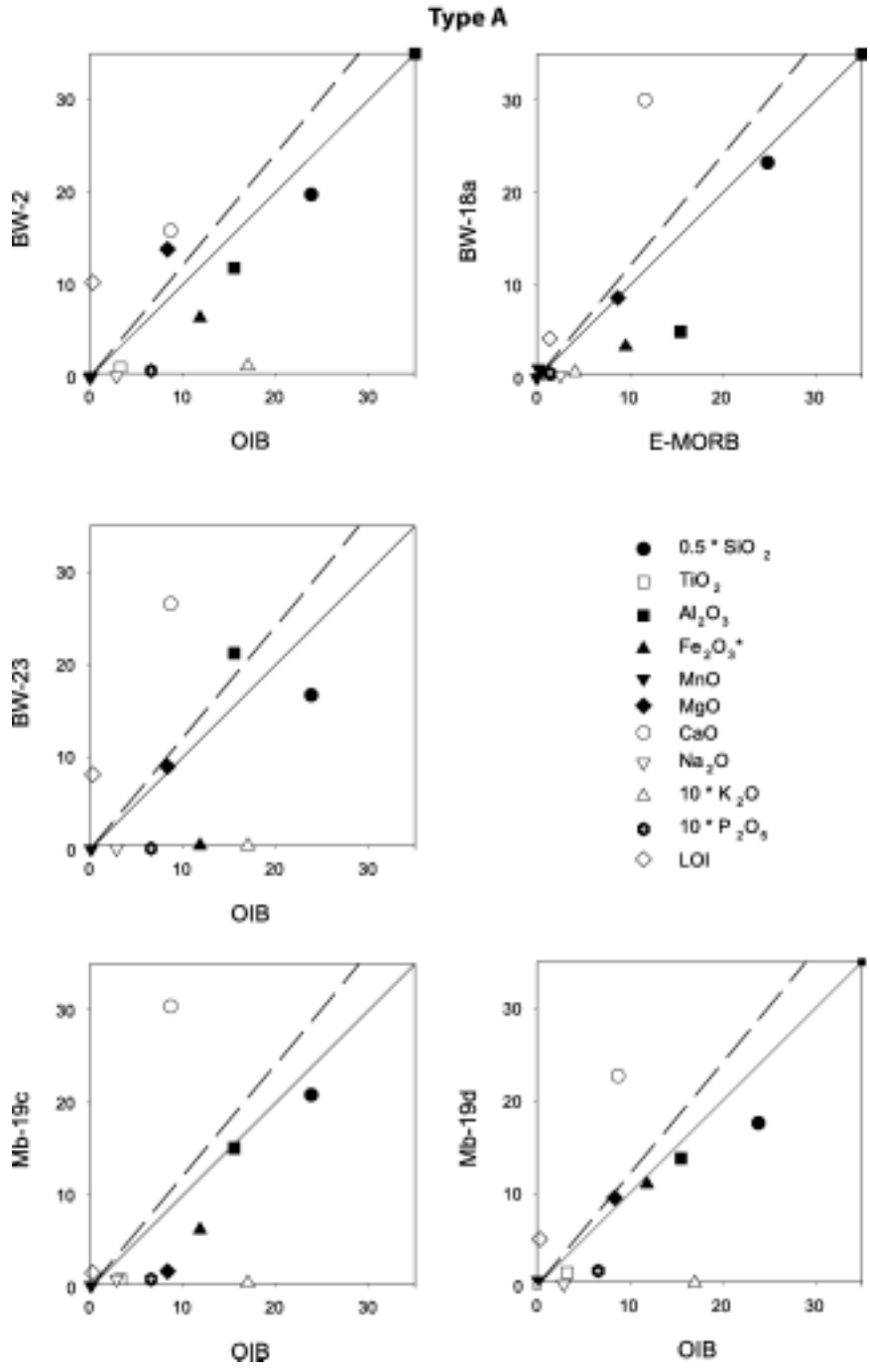


FIG. 10. Major-element isocon diagrams for representative samples of type A rodingites plotted against the composition of average OIB or E-MORB values. All values are given in wt%. Solid line represents constant mass assumption; dashed line assumes constant volume metasomatism.

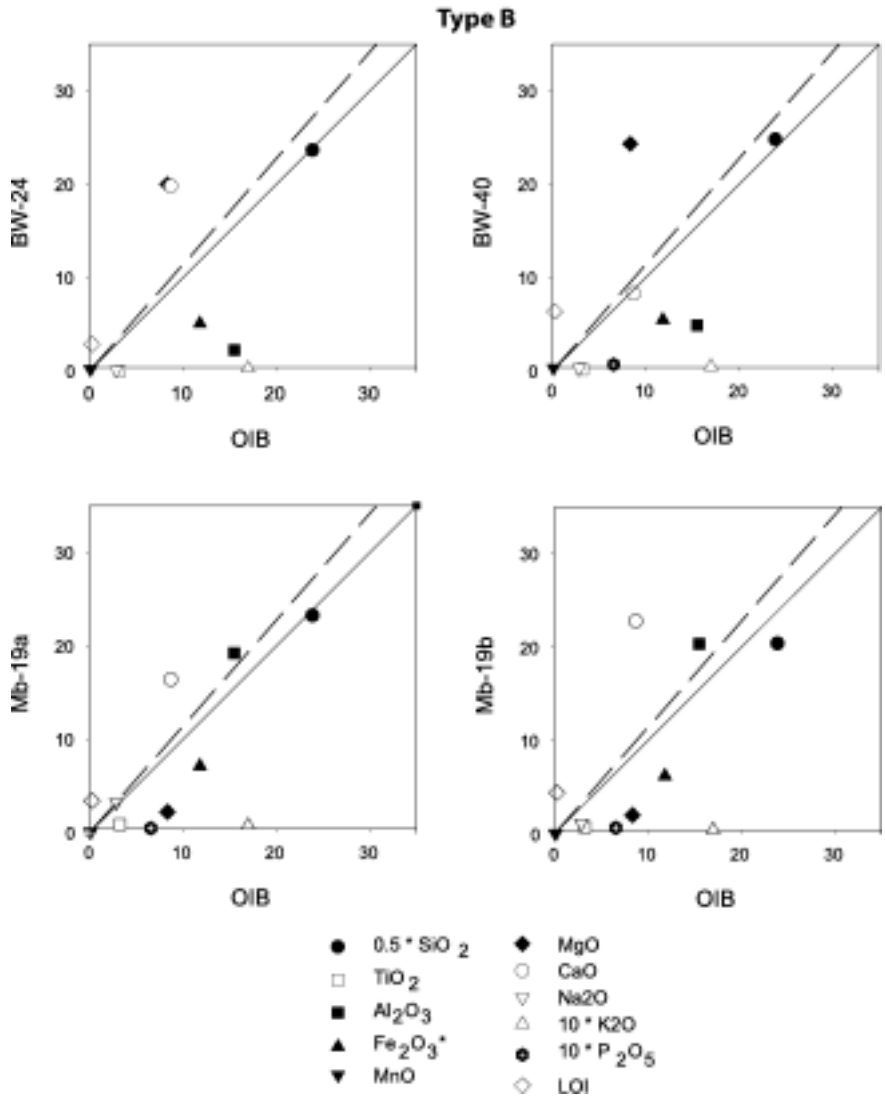


FIG. 11. Major-element isocon diagrams for representative samples of type B metasomatites plotted against the composition of average OIB values. All values are given in wt%. Solid line represents constant mass assumption; dashed line assumes constant volume metasomatism.

of phases in the reaction fronts towards these serpentinites (Brady, 1977; Winter, 2001).

The above data also shed some light on the relative mobility of the various elements during Ca-metasomatism. Ca, Na, K, Ti, P, Rb, Sr, and Ba (± Mg) are clearly the most mobile elements, whereas Zr and Y (± Nb) seem to have been least affected by metasomatism. Elements such as Si, Al, Fe, Cr, V, and Ni were variably mobilized (mostly leached out of the metabasalts), but to a much lesser extent than elements like Ca and the alkalis. These results are broadly consistent with theoretical and empirical data on the mobility of major and trace elements, with the exception of the behavior of Ti and P. It should be noted that although metasomatism resulted in the loss of some Nb relative to Zr and Y, the conclusions drawn on the protolith of these rocks from the Nb–Zr–Y diagram of Meschede

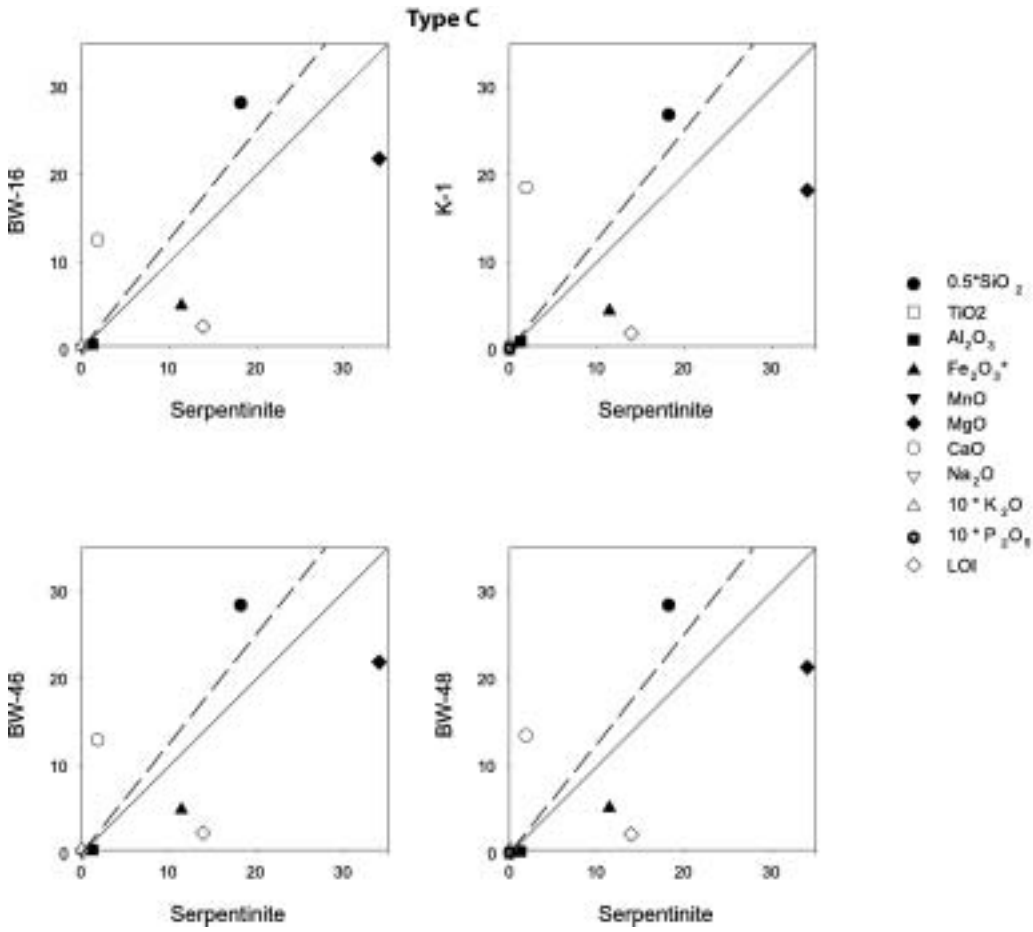


FIG. 12. Major-element isocon diagrams for representative samples of type C nephrites plotted against the composition of average serpentinites from the same area. All values are given in wt%. Solid line represents constant mass assumption; dashed line assumes constant volume metasomatism.

(1986) are still valid, inasmuch as the effect is small (Figs. 13 and 14) and because an increase in Nb relative to Zr and Y would only move some data points from the field of oceanic-island tholeiites into that of oceanic-alkali basalts (Fig. 7).

*Metasomatic fluid composition*

The microthermometric data presented above can be used to provide insight into the composition of the metasomatic fluid. Although these data were collected for only one sample (BW-39), they are nevertheless valuable given that BW-39 is a brecciated quartzite with a significant amount of Tr and Hgt (Table 2), and is one of several samples that appear to be transitional between quartzites and rodingites or nephrites (e.g., BW-50, BW-35, BW-36). Moreover, measurements were carried out on texturally early fluid inclusions (isolated or in clusters) in recrystallized quartz close to tremolite, so the fluid must have been trapped during some stage of metasomatism.

Eutectic melting temperatures ($Tm_e$) recorded for the fluid inclusions, which range from –19.8 to –56.6°C but cluster around –40°C suggest that these inclusions are filled with an aqueous fluid containing a mixture of NaCl and chlorides of divalent cations as $Mg^{2+}$ and $Ca^{2+}$ (Goldstein and Reynolds, 1994). The final melting temperatures ($Tm_f$) recorded for the same inclusions, which cluster mostly between –3.4 and 0°C (Fig. 6), indicate that

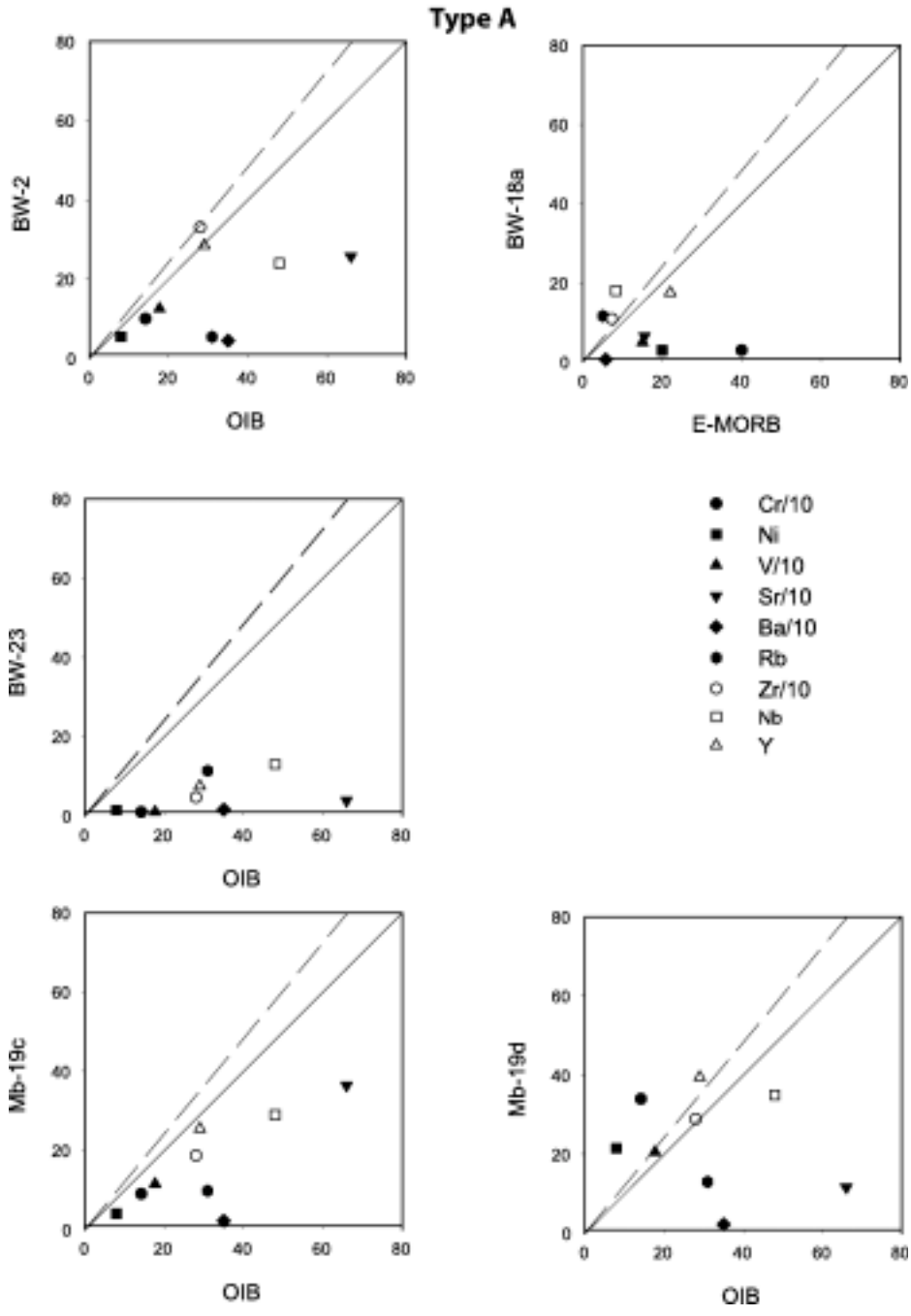


FIG. 13. Trace-element isocon diagrams for representative samples of type A rodingites plotted against the composition of average OIB or E-MORB values. All values are given in ppm. Solid line represents constant mass assumption; dashed line assumes constant volume metasomatism.

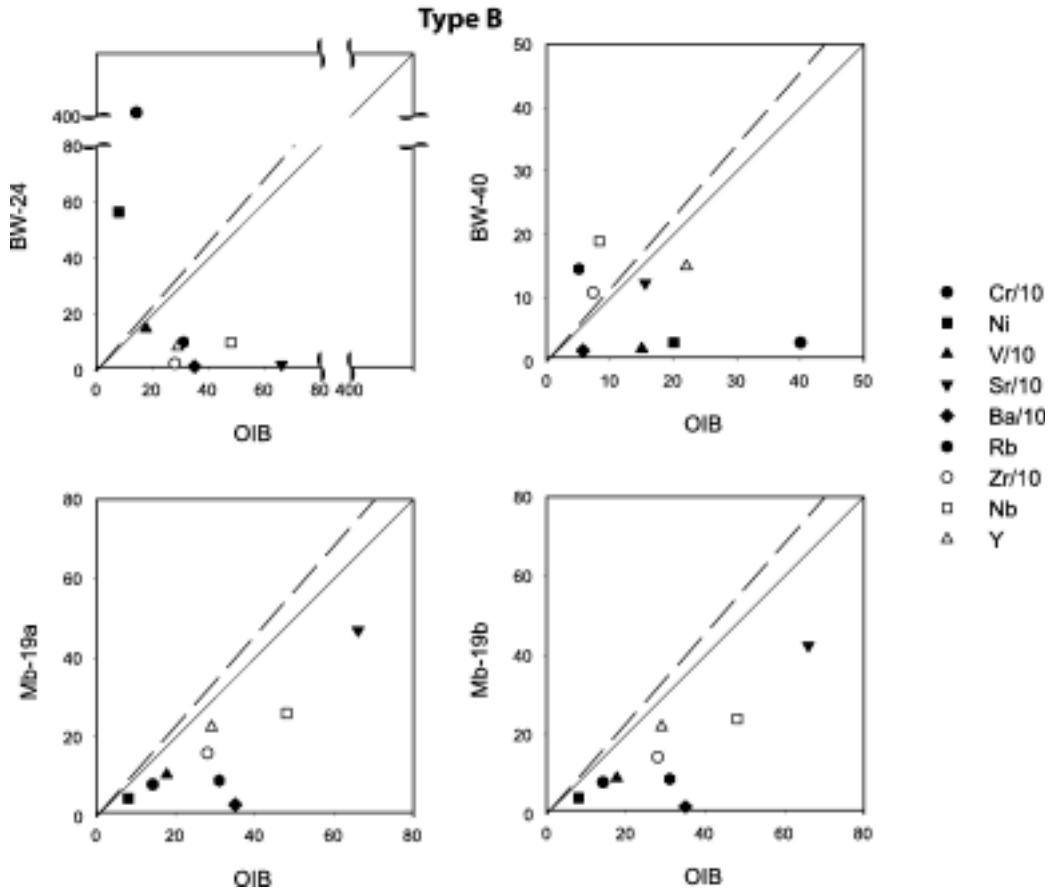


FIG. 14. Trace-element isocon diagrams for representative samples of type B metasomatites plotted against the composition of average OIB values. All values are given in ppm. Solid line represents constant mass assumption; dashed line assumes constant volume metasomatism.

the salinity of the aqueous fluids was ≤ 5.47 wt% NaCl equivalent, although a few outliers suggest that some inclusions contain a higher salinity fluid (~12 wt% NaCl equivalent).

On the other hand, homogenization temperatures ($T_h$) recorded for the same inclusions fall into three distinct groups: 130–160°C, 170–210°C, and 220–240°C. This overall scatter in $T_h$ values could be due to the entrapment of fluids at three or more different temperature conditions corresponding to the protracted range under which quartz recrystallized during metasomatism. Alternatively, the scatter could be interpreted as resulting from post-entrapment modification of inclusions, such as stretching during the exhumation of these blocks (e.g., Bodnar et al., 1989; Barker, 1995; Vityk and Bodnar, 1995; El-Shazly and Sisson, 1999, 2004). More microthermometric data are needed to better understand the reasons behind this scatter. It is worth noting that the microthermometric data presented here are quite similar to those of Schandl et al. (1990) for primary inclusions in diopside from rodingites from the Bowman asbestos mine area, Ontario, Canada.

## Petrogenesis

### *Mineral parageneses*

Understanding the petrogenesis of the samples described in this study is quite challenging, given their very fine grained nature, and the interplay between metamorphism and metasomatism. A successful petrogenetic interpretation therefore hinges

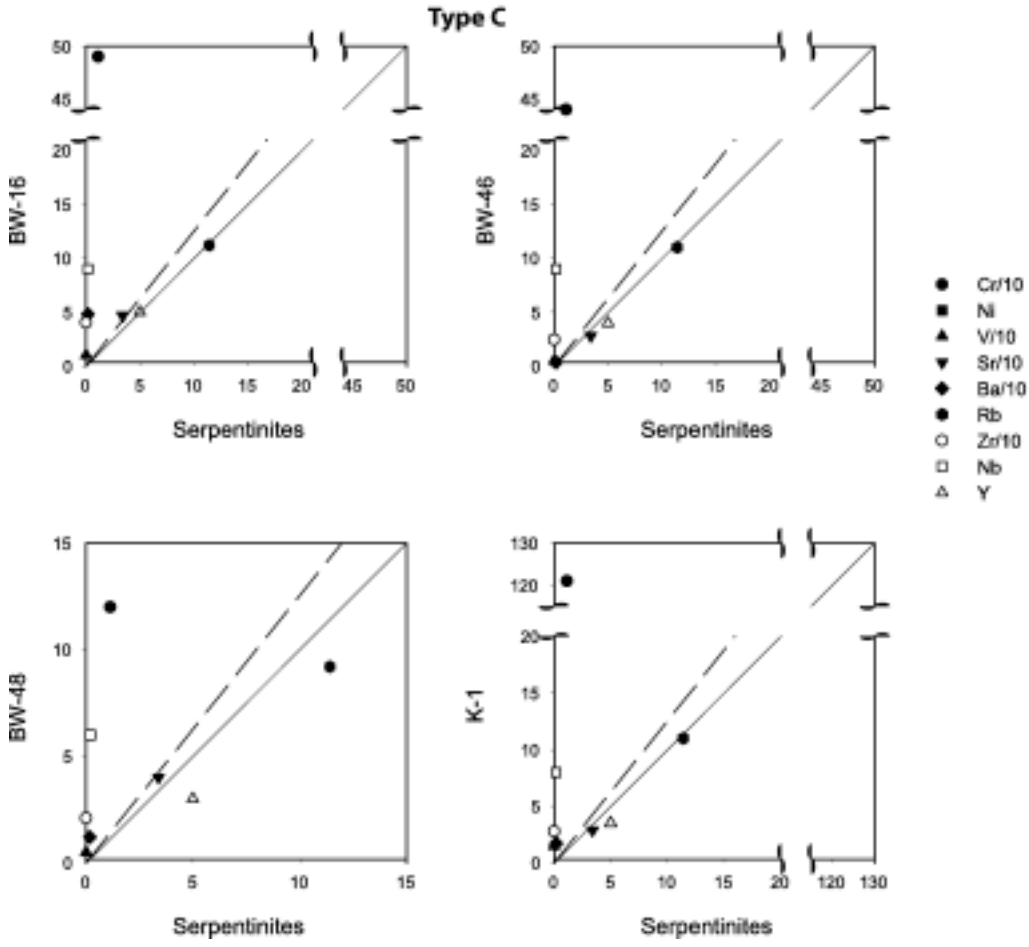


FIG. 15. Trace-element isocon diagrams for representative samples of type C nephrites plotted against the composition of average serpentinite values from the study area. All values are given in ppm. Solid line represents constant mass assumption; dashed line assumes constant volume metasomatism.

on our ability to identify specific equilibrium mineral assemblages (and their P-T stability ranges), and to relate each to a specific stage in the history of the sample. This is best accomplished by reasonable interpretations of the field relations, careful textural analysis, and suitable chemographic projections.

The serpentinite matrix mélange (SMM) enclosing the Ca-metasomatites is sandwiched between the overthrust metamorphosed muddy matrix mélange (MMM) and the underlying continental shelf units metamorphosed under high P/T. Although high P/T mineral assemblages have not been reported from the MMM in the Bawshir–Al-Khuwair area, muddy matrix mélanges that occupy the same structural position in other areas (e.g., Ruwi and Hamiriya to the east, and Saal to the west) contain Fe-Mg carpholite in the metasediments and Pmp + Chl + Lw/Act in some metabasalts, clearly indicating their high P/T origin (e.g., Goffé et al., 1988; El-Shazly, 1994, 1995). Therefore both the MMM and the SMM with their metasomatic blocks in Bawshir and Al-Khuwair may have also been affected by high P/T metamorphism. The occurrence of Pmp and its partial replacement by Hgt + Di ± Tr in a few samples (e.g., Mb-19a and BW-1) suggests that high-P/T metamorphism either preceded or overlapped with Ca-metasomatism.

Equilibrium mineral assemblages forming at different stages of evolution of these Ca-metasomatites can be illustrated with the help of suitable

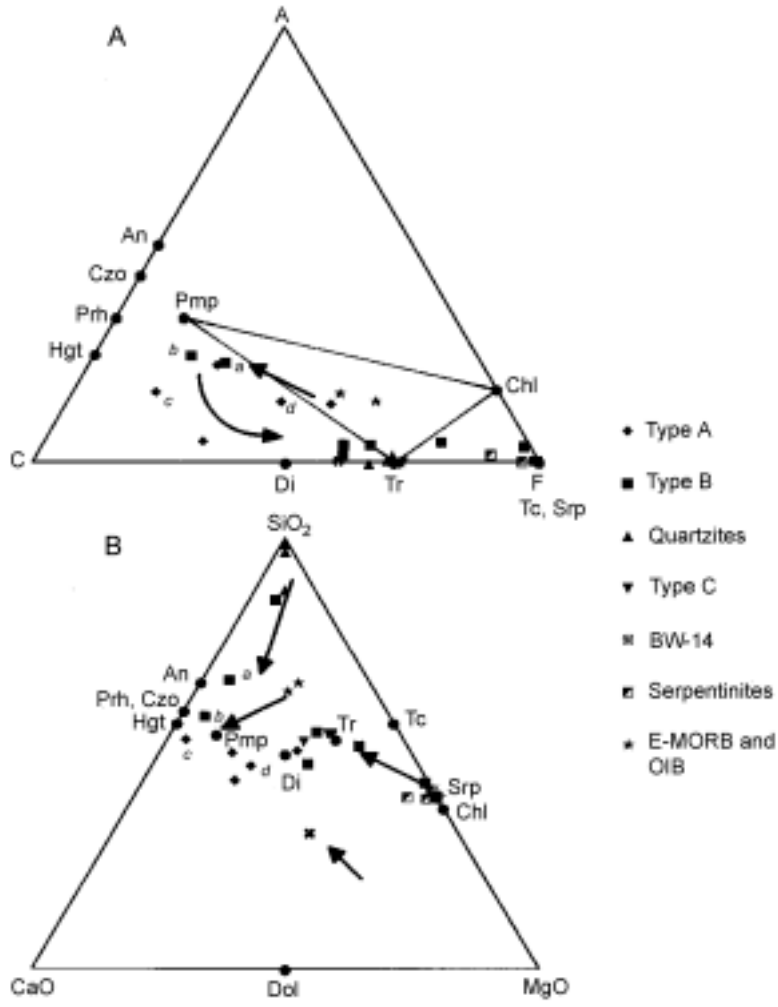


FIG. 16. Different types of metasomatites plotted on (A) ACF diagram, and (B) $SiO_2$–MgO–CaO ternary. Italicized letters "a" through "d" are labels for samples Mb-19a through Mb-19d. Solid arrows represent the chemical changes accompanying the transformation of metabasalts to types A and B metasomatites, or the serpentinites and ophidolomite to nephrites and calcareous schists, respectively.

chemographic projections. Since all metasomatic samples studied are broadly mafic, their mineral assemblages are best represented by the ACF ternary diagram (Fig. 16A). The CaO–$SiO_2$–MgO ternary (Fig. 16B) is also useful for monitoring metasomatic changes because these three components appear to be the ones most readily exchanged between the tectonic blocks and their host serpentinites. Both plots show that type A rodingites are generally more enriched in CaO and depleted in $SiO_2$ than type B metasomatites, whereas type C nephrites have the lowest $Al_2O_3$ and highest MgO values among the three metasomatites. Figure 16 also shows that an OIB or E-MORB protolith plots within the compositional range of the assemblage Pmp–Chl–Tr or Pmp–Tr–Ab, and is hence compatible with the mineral assemblage observed in several blocks from the Ruwi–Hamiriya area (e.g., R-85, R-77; El-Shazly, 1994).

Assuming that the basaltic protoliths of all type A and B metasomatites were originally metamorphosed under high-P, low-T conditions (3–6 kbar,

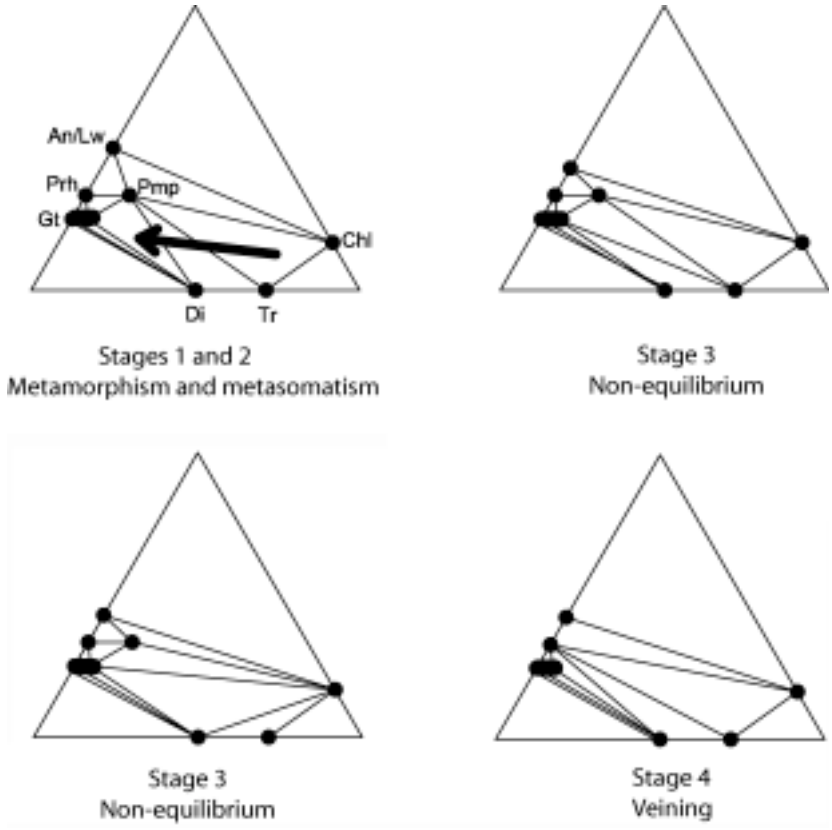


FIG. 17. ACF diagrams showing the mineral assemblages characteristic of the four different stages of metasomatism. Arrow on the first diagram shows the effects of metasomatism on mineral assemblages during high P/T metamorphism, without any changes in P and T (Stages 1 and 2). Note that the assemblages of stage 3 are all metastable.

T < 310°C; El-Shazly, 1994, 1995, 1996), then the most common mineral assemblage for an OIB or E-MORB would have been Pmp–Chl–Act/Tr–Ab (El-Shazly, 1994). Given the mineralogical and bulk-chemical compositions of samples Mb-19a-d, as well as those of other type A and B metasomatites, the following paragenetic sequence is inferred:

High P/T stage: Pmp + Chl + Tr + Ab.
Stage 1: Pmp + Tr + Di (BW-1, Mb-19a)
Stage 2: Pmp + Di + Hgt (Mb-19b)
Stage 3: Di + Hgt + Tr (Mb-19c) and Hgt + Chl ± Di (Mb-19d)
Stage 4 (veining): Tr + Prh ± Chl (BW-2; BW-18a).

This sequence (Figs. 16A and 17) would largely explain the metasomatic fronts developing between sample Mb-19a and the serpentinite, and would account for such textures as the replacement of Tr by Pmp in sample BW-1, and the late formation of Tr + Prh ± Chl in veins at the expense of earlier Di and Hgt (e.g., BW-50; Fig. 4E). On the other hand, assuming that type C nephrites were originally serpentinites, their formation entails the increased modal content of Tr ± Hgt/Gt at the expense of serpentine, and therefore requires the addition of CaO and $SiO_2$. Similarly, metasomatism of the quartzites requires the addition of CaO and MgO ± loss of $SiO_2$, whereas the calcareous schist (BW-14) probably formed by the addition of $SiO_2$ to an ophidolomite. These relations are shown schematically by arrows on Figure 16B.

### *P-T conditions of formation*

The P-T conditions of metasomatism are difficult to determine given the lack of appropriate thermo-

barometers and the fact that metasomatism appears to have occurred over a range of temperatures and pressures. Nevertheless, minimum and maximum conditions of P and T can be estimated for at least some of the observed mineral assemblages. The common occurrence of hydrogrossular and its persistence through several stages of evolution suggests metasomatic T of > 220°C (Carlson, 1956). The occurrence of prehnite + tremolite in late veins suggests relatively low temperatures for this stage (< 360°C according to Rice, 1983). The absence of idocrase from all samples including Mb-19c and BW-18a, which are sufficiently calcic for stabilizing this mineral (Fig. 16A) also supports a low T for all stages of metasomatism (< 320°C, Rice, 1983). The persistence of pumpellyite in some samples is consistent with this conclusion according to the results of Schiffman and Liou (1983) and Liou et al. (1985). The fact that chrysotile is the predominant serpentine mineral, and that this mineral was itself involved in some metasomatic process possibly leading to the formation of nephrites and some calcareous schists suggests a stage of metasomatism at T < 260°C and P < 5 kbar, according to the petrogenetic grids of Bucher and Frey (1994).

Another method for estimating P-T conditions of metasomatism is to calculate an activity-corrected petrogenetic grid for an appropriate chemical system using the compositions of the analyzed minerals. This method has the advantage of allowing one to constrain the P-T conditions for the different stages of metasomatism, and hence the P-T evolution of these rocks. However, extreme caution has to be taken when interpreting these grids because the bulk-rock composition progressively changes from one stage to another.

Most metasomatic blocks are adequately represented by the chemical system CaO–MgO–$Al_2O_3$–$SiO_2$–$H_2O$ (CMASH). A petrogenetic grid for this system was calculated for the end-members Di, Tr, Grossular (Gr), Clinochlore (Chl), Mg–Al pumpellyite (Pmp), Prh, Czo, Lw, and Qz, projected from $H_2O$, using program TWEEQU (v. 2.02) of Berman (1991) and Berman's (1988) thermodynamic data as given in his June 1992 data base. Activities of the components Gr, Di, Tr, Prh, and Chl were set at 1.0, 0.86, 0.6, 1.0, and 0.5, respectively, according to the average compositions of these minerals as listed in Tables 3–6. The activity of Pmp was set at 0.35 based on the analyses given in El-Shazly (1994), and assuming that this phase was mostly a product of high P/T metamorphism. Unit activity was assumed for $H_2O$ because our microthermometric measurements indicate that the fluids were highly aqueous with no $CO_2$. The activities of Lw, Qz, and Czo were also set at unity, inasmuch as these phases do not occur in our samples, and are useful only for setting upper and lower limits on P and T.

The calculated grid has 39 stable reactions and seven invariant points (in the P-T range 1–10 kbar, 100–500°C), and shows stability fields for the assemblages Pmp–Tr–Di and Pmp–Di–Gr (stages 1 and 2, Fig. 17), and for the assemblage Prh–Tr–Chl (stage 4). Although some quartz-absent reactions have probably played a role in the formation of some of our samples, their removal has little if any effect on the P-T estimates for the critical assemblages listed above, and facilitates the visual interpretation of this grid and the accompanying ACF diagrams. Figure 18 is a simplified version of this grid in which all quartz-absent invariant points and reactions were removed.

Figure 18 (see also Table 8) shows that the mineral assemblages Pmp–Di–Tr and Pmp–Gt–Di of stages 1 and 2 are stable over a relatively large P-T range of 3–6 kbar, T < 360°C, consistent with the above estimates for Ca-metasomatism. These conditions overlap considerably with those of high P/T metamorphism in the Ruwi area, where the assemblage Pmp – Tr – Chl and Pmp – Chl – Lw are stable (T < 310°C, P = 3–6 kbar; El-Shazly, 1994). With textures and reaction fronts for samples Mb-19a–d suggesting the replacement of Pmp by Di + Tr ± Hgt, it is reasonable to conclude that the assemblages Pmp–Tr–Chl (or Pmp–Chl–Lw for more aluminous samples) were the precursors of most metasomatic assemblages. This leads to the conclusion that metasomatic stages 1 and 2 may have been concomitant with high-P/T metamorphism. On the other hand, Figure 18 shows that the vein assemblage Prh–Tr–Chl characteristic of stage 4 is stable at P < 3.2 kbar, and T = 253–342°C, as constrained by reactions 15 and 22. The occurrence of Ep + Chl in a few metasomatized quartzites (e.g., BW-39; Table 1), suggests that metasomatic temperatures must have exceeded those of reaction 4 (Fig. 18) during some stage (probably stages 3–4; Fig. 17). On the other hand, the absence of the assemblage Czo + Di from all samples indicates that metasomatic temperatures remained below 370°C, as constrained by reaction 21 (Fig. 18). Isochores calculated for the fluid inclusions analyzed in this study (dashed lines of Fig. 18) yield additional constraints on P-T conditions, inasmuch as the P-T path of the metasomatic blocks

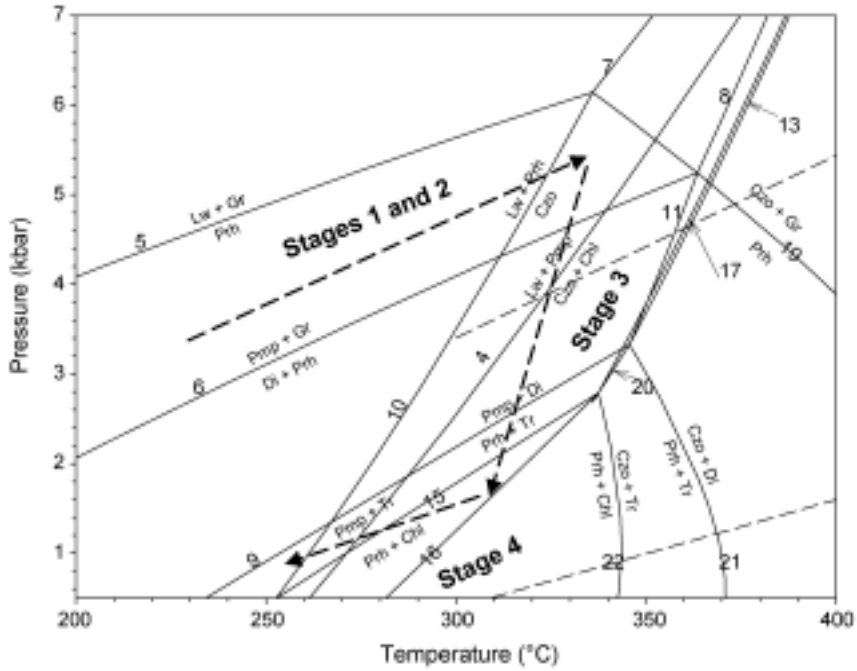


FIG. 18. Activity-corrected petrogenetic grid for the system CMASH calculated for the end-members Di, Tr, grossular (Gt), chlinochlore (Chl), Mg–Al pumpellyite (Pmp), Prh, Czo, Lw, and Qz, projected from $H_2O$, using program TWEEQU (v. 2.02) of Berman (1991) and Berman's (1988) thermodynamic data. The activities of the components Pmp, Di, Tr, and Chl were set at 0.35, 0.86, 0.6, and 0.5, respectively; unit activity was assumed for all other components. All quartz-absent reactions were removed for the sake of simplicity. Dashed lines represent the entire range of isochores calculated for the fluid inclusions of BW-39 using the equation of Zhang and Franz (1987). Dashed arrows represent a possible P-T path of evolution of the various blocks. A complete list of the reactions shown is given in Table 8.

must have followed these isochores during its latest stages in order to preserve such inclusions. Overall, these relations suggest that the P-T evolution during metasomatism may have followed a path similar to that outlined by the curved arrow in Figure 18.

However, the calculated grid does not show a stability field for the assemblages Gr–Di–Tr or Gr–Di–Chl of stage 3 (Fig. 17). In fact, the thermodynamic data used in the calculation of Figure 18 indicate that the reaction Pmp + Di = Gr + Tr necessary for the formation of stage 3 assemblages is metastable at all P-T conditions. This discrepancy could be due to inappropriate thermodynamic data or solution models, particularly since the stable garnet is a hydrogrossular in most samples, whereas the grid was calculated assuming pure grossularite. Alternatively, these two assemblages may indeed be metastable, their occurrence being a function of lack of equilibration between the metasomatizing fluids and the metabasaltic blocks. Although Hgt, Di, and Tr appear to be in textural equilibrium in some samples, we favor the explanation that Tr was not in equilibrium with Hgt and Di, in line with the replacement textures in some quartzites (Fig. 4D) and the conclusions of Coleman (1967), Leblanc and Lbouabi (1988), and Schandl et al. (1989), who suggested that Tr crystallization post-dates that of Hgt and Di in most rodingites, and is confined to reaction zones near the serpentinite.

## Stages of Metasomatism and Tectonic Implications

Understanding the origin and evolution of Ca-metasomatites requires integrating the data presented above with the petrological, geochemical, geochronological, and structural data available for the Saih Hatat area (particularly the upper plate rocks; Goffé et al., 1988; Le Métour et al., 1990; El-Shazly, 1994, 1995, 1996; Miller et al., 1998;

TABLE 8: List of Reactions Shown in Figure 18[1]

| Reaction no. | Reaction |
|---|---|
| 1 | 15 Lw + 11 Di = 6 Pmp + 8 Qz + Tr + 8 $H_2O$ |
| 2 | Qz + Pmp = Di + Lw + Czo + $H_2O$ |
| 3 | 86 Lw + 17 Tr = 95 Qz + 30 Pmp + 11 Chl + 40 $H_2O$ |
| 4 | 14 Lw + 5 Pmp = 17 Czo + 4 Qz + Chl + 33 $H_2O$ |
| 5 | Qz + Lw + Gr = 2 Prh |
| 6 | 7 Qz + 2 Pmp + 4 Gr + 2 $H_2O$ = 2 Di + 9 Prh |
| 7 | Gr + 5 Lw = 4 Czo + Qz + 8 $H_2O$ |
| 8 | Gr + 5 Pmp + 4 Qz = 9 Czo + 5 Di + 13 $H_2O$ |
| 9 | 13 Qz + 6 Pmp + 14 Di = 15 Prh + 4 Tr + 2 $H_2O$ |
| 10 | 2 Lw + Prh = 2 Czo + Qz + 4 $H_2O$ |
| 11 | Qz + 2 Pmp + Prh = 2 Di + 4 Czo + 6 $H_2O$ |
| 12 | 4 Lw + 5 Pmp + 3 Qz = 11 Czo + Tr + 19 $H_2O$ |
| 13 | 9 Pmp + 7 Qz = 15 Czo + Tr + 4 Di + 23 $H_2O$ |
| 14 | 5 Di + 9 Lw = 6 Czo + Tr + 2 Qz + 14 $H_2O$ |
| 15 | 3 Tr + 6 Qz + 20 Pmp = 7 Chl + 43 Prh + 2 $H_2O$ |
| 16 | 3 Qz + 5 Pmp = Chl + 7 Prh + 3 Czo + 5 $H_2O$ |
| 17 | 2 Chl + 25 Pmp + 29 Qz = 43 Czo + 7 Tr + 67 $H_2O$ |
| 18 | 10 Lw + Tr = 6 Czo + 7 Qz + Chl + 14 $H_2O$ |
| 19 | 2 Czo + 3 Qz + 2 Gr + 4 $H_2O$ = 5 Prh |
| 20 | 5 Pmp + 5 Qz = 7 Czo + Tr + 2 Prh + 11 $H_2O$ |
| 21 | 6 Czo + 5 Qz + 10 Di + 8 $H_2O$ = 9 Prh + 2 Tr |
| 22 | 4 Czo + Tr + 6 $H_2O$ = Chl + 5 Prh + 2 Qz |

[1]Assemblages on the left are stable on the high-P side of the reaction, or on the low-T side for nearly vertical curves. Note that reactions 1, 2, 3, 12, 14, 18, 19, and 20 plot outside the P-T range of Figure 16.

El-Shazly et al., 2001). Accordingly, the stages of development of these metasomatites need to be interpreted in the context of the tectonic evolution of northeastern Oman. For this purpose, the reader is referred to the tectonic model of El-Shazly et al. (2001), which we use as a reference frame.

Intraoceanic thrusting during the Late Cretaceous facilitated serpentinization of the lithospheric mantle peridotites (which later constituted ~65% of the Semail ophiolite) along the thrust plane. As the overriding plate moved southwest toward the Oman continental margin, basaltic seamounts of the Hawasina basin with their carbonate deposits and cherts were detached from the underthrust plate and incorporated as blocks into serpentinites forming at the base of the overriding plate, giving rise to a mélange. As the ophiolite advanced towards the continental margin, several slivers of shale or mud from the Hawasina and/or Muti foreland basins, or the foundering continental shelf were caught beneath the ophiolite to form another mélange (MMM). Both the MMM and SMM along with their enclosed blocks of chert, limestone, and basalt were eventually metamorphosed under pumpellyite-actinolite– to lawsonite-albite–facies conditions (3–6 kbar, T < 310°C; El-Shazly, 1995, 1996) under the influence of the overriding ophiolite, which may have reached a thickness of 21 km (e.g., Hopson et al., 1981).

Serpentinization of the basal peridotites probably began shortly after intraoceanic detachment (as soon as the T in the overriding plate dropped below 600°C) and continued throughout the above stages, resulting in the release of $Ca^{2+}$ according to the reactions:

$$2Mg_2SiO_4 + H_2O + 2\,H^+ = Mg_3Si_2O_5(OH)_4 + Mg^{2+} \quad (1)$$

$$2Mg_2Si_2O_6 + H_2O + 2\,H^+ = Mg_3Si_2O_5(OH)_4 + 2SiO_2 + Mg^{2+} \quad (2)$$

$$CaMgSi_2O_6 + 2Mg^{2+} + 3H_2O = Mg_3Si_2O_5(OH)_4 + Ca^{2+} + 2\,H^+. \quad (3)$$

$Ca^{2+}$, $Mg^{2+}$, $\pm$ $SiO_2$ released from the peridotites diffused into basalt and chert blocks, resulting in their metasomatism. Early stages of this process were probably concomitant with high-P/T metamorphism, and caused formation of the mineral assemblage Pmp–Tr–Di primarily at the expense of igneous plagioclase, according to reactions similar to:

$$5\,CaAl_2Si_2O_8 + 2\,Mg^{2+} + 3\,Ca^{2+} + SiO_2 + 12\,H_2O = 2\,Ca_4MgAl_5Si_6O_{23}(OH)_3.2H_2O + 10\,H^+ \quad (4)$$

$$2\,CaAl_2Si_2O_8 + 5\,Mg^{2+} + 4\,SiO_2 + 2\,H^+ = Ca_2Mg_5Si_8O_{22}(OH)_2 + 4\,Al^{3+}. \quad (5)$$

Continued metasomatism at the same P-T conditions (3–6 kbar; 220–310°C) formed the assemblage Pmp –Hgt–Di (stage 2; Fig. 17) according to reactions similar to:

$$3\,Ca_2Mg_5Si_8O_{22}(OH)_2 + 16\,Al^{3+} + 18\,Ca^{2+} + 24\,H_2O = 8\,Ca_3Al_2Si_3O_{12} + 15\,Mg^{2+} + 54\,H^+. \quad (6)$$

The development of the non-equilibrium assemblages Hgt–Di–Tr and Hgt–Di–Chl as reaction fronts and zones characteristic of stage 3 probably involved the addition of $Mg^{2+}$ to some metabasalts. This $Mg^{2+}$ could have been provided by reactions similar to (6) above, the continued serpentinization of olivine and orthopyroxene in the peridotites (after the consumption of Cpx), or the conversion of serpentine to talc + magnesite according to the reaction:

$$2\,Mg_3Si_2O_5(OH)_4 + 2\,CO_2 + 2\,H^+ = Mg_3Si_4O_{10}(OH)_2 + 2\,MgCO_3 + 2\,H_2O + Mg^{2+}. \quad (7)$$

The common occurrence of magnesite veins and pods as well as some talc in the serpentinites supports this hypothesis.

In contrast, type C nephrites formed at the expense of serpentinites at their contacts with quartzites by reactions similar to:

$$2\,Mg_3Si_2O_5(OH)_4 + 2\,Ca^{2+} + 4\,Si^{4+} + 6\,H_2O = Ca_2Mg_5Si_8O_{22}(OH)_2 + 18\,H^+ + Mg^{2+} \quad (8)$$

through the diffusion of $Si^{4+}$ from the quartzites aided by the infiltration of aqueous fluids. The $Ca^{2+}$ necessary for the completion of this process was probably produced by earlier serpentinization of peridotites. The P-T conditions prevailing during stage 3 are difficult to constrain, given the lack of appropriate equilibrium mineral assemblages.

Final emplacement of the ophiolite onto the continental margin ~78 Ma was followed by the initiation of exhumation of all high-P/T metamorphic rocks (El-Shazly et al., 2001). This caused the tectonic mélanges to be exhumed to depths of 10 km or less, where several enclosed blocks fractured, brecciated, and developed numerous veins filled with Prh + Chl + Tr (stage 4; Fig. 17). P-T conditions for this stage are estimated at 280–340°C and P < 2.7 kbar, as constrained by the petrogenetic grid of Figure 18. During or shortly after fracturing, quartz crystals in the brecciated metacherts trapped some of the metasomatizing fluid in inclusions. Preservation of these fluid inclusions requires the P-T path of the metasomatic blocks to have a segment follow the isochores calculated for the fluid in these inclusions (dashed lines; Fig. 18). This in turn suggests that during their latest stage of evolution, the metasomatic blocks underwent near-isobaric cooling. Figure 18 shows a possible P-T path for the rodingites and Ca-metasomatites of Bawshir–Al-Khuwair, although it should be emphasized that this path is purely schematic and somewhat speculative given that the P-T conditions of stage 3 are not well known.

## Summary and Conclusions

1. The MMM and SMM probably represent slivers of the Hawasina basin caught between the overriding ophiolite and the continental margin; both were metamorphosed under high P and very low T.

2. Types A and B rodingites and Ca metasomatites in SMM were originally ocean island basalts, whereas type C nephrites represent reaction zones forming at the expense of serpentinites.

3. Metasomatism of the metabasalts involved the addition of CaO and volatiles, and the removal

of $SiO_2$, $Al_2O_3$, $Fe_2O_3$*, and alkalis. Most trace elements were also removed during this process, with minimal effect on Zr, Y, and Nb.

4. Metasomatism occurred in four stages, the earliest of which was characterized by the introduction of $Ca^{2+}$ into the basaltic and chert blocks, and took place at P = 3–6 kbar, T = 220–310°C, penecontemporaneously with high-P/T metamorphism and serpentinization at depth. Later stages involved the addition of $Mg^{2+}$ to these blocks and the formation of nephrites, and may have coincided in part with near-surface alteration of some serpentine to talc and magnesite at P < 3 kbar; T ~ 280–310°C.

5. The main mechanism of Ca- (± Mg and Si) metasomatism and bimetasomatism was diffusion, particularly at depth during subduction. However, infiltration of an aqueous, low-salinity fluid played an important role in metasomatism at shallow depths after considerable exhumation.

## Acknowledgments

This paper is written in honor of Bob Coleman who introduced El-Shazly to Oman, the problems of high-P/T metamorphism, and metasomatism in Saih Hatat, one of the outcrops mapped in this study. El-Shazly is exceedingly grateful to Bob for guidance, advice, and friendship. Part of this study constituted the senior thesis of M. Al-Belushi, prepared in partial fulfillment of his B.Sc. degree at Sultan Qaboos University. The authors are grateful to Prof. T. Labotka for XRD analyses at the University of Tennessee, Knoxville, and to Dr. V. B. Sisson for the use of the heating-freezing stage at Rice University. The authors also acknowledge the assistance of Khalifa Al-Busaidi, Syed Assim, Saif Al-Maamari, and Samira Al-Kharousi with thin-section preparation and SEM and XRF analysis at Sultan Qaboos University. Dr. Hilal Al-Azri, Director General of the Geological Survey, Ministry of Industry and Commerce, Oman, is thanked for facilitating fieldwork for El-Shazly over the years. Dr. Jeff Rogers is thanked for drafting Figure 1. This study was financially supported in part by a research grant from the Office of Research, Grants and Contracts, University of Tennessee at Martin. This paper benefited from very careful and constructive reviews by Drs. G. E. Harlow, T. Labotka, and V. B. Sisson. Any remaining errors are the sole responsibility of the authors.

## REFERENCES

Afifi, A. M., and Essene, E. J., 1988, MINFILE: A microcomputer program for storage and manipulation of chemical data on minerals: American Mineralogist, v. 73, p. 446–447.

Barker, A. J., 1995, Post-entrapment modification of fluid inclusions due to overpressure: Evidence from natural samples: Journal of Metamorphic Geology, v. 13, p. 737–750.

Barnes, I., and O'Neil, J. R., 1969, The relationship between fluids in some fresh alpine type ultramafics and possible modern serpentinization: Geological Society of America Bulletin, v. 80, p. 1947–1960.

Barriga, F., and Fyfe, W. S., 1983, Development of rodingites in basaltic rocks in serpentinites, East Liguria, Italy: Contributions to Mineralogy and Petrology, v. 84, p. 146–151.

Berman, R. G., 1988, Internally consistent thermodynamic data for minerals in the system $Na_2O$–$K_2O$–CaO–MgO–FeO–$Fe_2O_3$–$Al_2O_3$–$SiO_2$–$TiO_2$–$H_2O$–$CO_2$: Journal of Petrology, v. 29, p. 445–522.

_____, 1991, Thermobarometry using multi-equilibrium calculations: A new technique, with petrological applications: Canadian Mineralogist, v. 29, p. 833–855.

Bilgrami, S. A., and Howie, R. A., 1960, The mineralogy and petrology of a rodingite dyke, Hindubagh, Pakistan: American Mineralogist, v. 45, p. 791–801.

Bodnar, R. J., Binns, P. R., and Hall, D. L., 1989, Synthetic fluid inclusions—VI. Quantitative evaluation of the decrepitation behavior of fluid inclusions in quartz at one atmosphere confining pressure: Journal of Metamorphic Geology, v. 7, p. 229–242.

Brady, J., 1977, Metasomatic zones in metamorphic rocks: Geochmica et Cosmochimica Acta, v. 41, p. 113–125.

Bryndzia, L. T., and Scott, S. D., 1987, The composition of chlorite as a function of sulfur and oxygen fugacity: An experimental study: American Journal of Science, v. 287, p. 50–76.

Bucher, K., and Frey, M., 1994, Petrogenesis of metamorphic rocks: Berlin, Germany, Springer Verlag, 318 p.

BVSP (Basaltic Volcanism Study Project), 1981, Basaltic volcanism on the terrestrial planets: New York, NY, Pergamon Press, 1286 p.

Capedri, S., Garuti, G., and Rossi, A., 1978, Rodingites from Pindos: Constraints on the "rodingite problem": Neus Jahrbuch Mineralogie Abhandlungen, v. 3, p. 242–263.

Carlson, E. T., 1956, Hydrogranet formation in the system lime–alumina–silica–water: U. S. National Bureau of Standards Journal of Research, v. 56, p. 327–335.

Coleman, R. G., 1967, Low temperature reaction zones and alpine ultramafic rocks of California, Oregon, and Washington: U.S. Geological Survey Bulletin, v. 1247, p. 1–49.

Cox, K. G., Bell, J. D., and Pankhurst, R. J., 1979, The interpretation of igneous rocks: London, UK, George Allen and Unwin, 450 p.

El-Shazly, A. K., 1994, Petrology of lawsonite, pumpellyite and sodic amphibole-bearing rocks from Saih Hatat, NE Oman: Journal of Metamorphic Geology, v. 12, p. 23–48.

_____, 1995, Petrology of Fe-Mg carpholite-bearing metasediments from NE Oman: Journal of Metamorphic Geology, v. 13, p. 379–396.

_____, 1996, Petrology of Fe-Mg carpholite-bearing metasediments from NE Oman: Reply to comments by Vidal and Theye: Journal of Metamorphic Geology, v. 14, p. 386–397.

El-Shazly, A. K., Brocker, M., Hacker, B., and Calvert, A., 2001, Formation and exhumation of blueschists and eclogites from NE Oman: New constraints from Rb-Sr and $^{40}Ar/^{39}Ar$ dating: Journal of Metamorphic Geology, v. 19, p. 233–248.

El-Shazly, A. K., and Coleman, R. G., 1990, Metamorphism in the Oman Mountains in relation to the ophiolite emplacement, *in* Robertson, A. H. F., Searle, M. P., and Ries, A., eds., The geology and tectonics of the Oman Region: Geological Society of London, Special Publication, v. 49, p. 475–495.

El-Shazly, A. K. and Sisson, V. B., 1999, Retrograde evolution of eclogites and blueschists from NE Oman: Evidence from fluid inclusions and petrological data: Chemical Geology, v. 154, p. 193–223.

_____, 2004, Fluid inclusions in carpholite-bearing metasediments and blueschists from NE Oman: Constraints on P-T evolution: European Journal of Mineralogy, v. 16, p. 221–233.

El-Shazly, A. K., Worthing, M. A., Jayawardane, J., and Varne, R., 1994, Geochemistry of metamorphosed mafic rocks from Saih Hatat: Insights into the preobduction history of NE Oman: Journal of the Geological Society of London, v. 151, p. 999–1016.

Floyd, P. A., and Winchester, J. A., 1975, Magma type and tectonic setting discrimination using immobile elements: Earth and Planetary Science Letters, v. 27, p. 211–218.

Frantz, J., D. and Mao, H. K., 1979, Bimetasomatism resulting from intergranular diffusion: II. Prediction of multimineralic zone sequences: American Journal of Science, v. 279, p. 302–232.

Grauch, R. I., 1989, Rare earth elements in metamorphic rocks, *in* Lipin, B. R., and McKay, G. A., eds., Geochemistry and mineralogy of rare earth elements: Reviews in Mineralogy, v. 21, p. 147–168.

Glennie, K. W., Boeuf, M. G. A., Hughes Clark, M. H. W., Moody-Stuart, M., Pilaar, W. F., and Reinhardt, B. M., 1974, Geology of the Oman mountains: Verhandelingen van het Koninklijk Nederlands Geologischs Mijnbouwkundig Genootschap, v. 31, p. 1–423.

Goffé, B., Michard, A., Kienast, J. R., and Le Mér, O., 1988, A case of obduction-related high-P low-T metamorphism in upper crustal nappes, Arabian continental margin, Oman: P-T paths and kinematic interpretation: Tectonophysics, v. 151, p. 363–386.

Goldstein, R. H., and Reynolds, T. J., 1994, Systematics of fluid inclusions in diagenetic minerals: SEPM Short Course, v. 31, 199 p.

Grant, J. A., 1986, The isocon diagram: A simple solution to Gresen's equation for metasomatic alteration: Economic Geology, v. 81, p. 1976–1982.

Gregory, R. T., Gray, D. R., and Miller, J. M., 1998, Tectonics of the Arabian margin associated with the formation and exhumation of high pressure rocks, Sultanate of Oman: Tectonics, v. 17, p. 657–670.

Hall, A., and Ahmed, Z., 1984, Rare earth content and origin of rodingites: Chemie der Erde, v. 43, p. 45–56.

Harlow, G. E., and Sorensen, S. S., 2004, Jade (nephrite and jadeitite) and serpentinite: Metasomatic connections: International Geology Review, v. 46, forthcoming.

Honnorez, J., and Kirst, P., 1975, Petrology of rodingites from the equatorial Mid-Atlantic fracture zones and their geotectonic significance: Contributions to Mineralogy and Petrology, v. 49, p. 233–257.

Hopson, C. A., Coleman, R. G., Gregroy, R. T., Pallister, J. S., and Bailey, E. H., 1981, Geologic section through the Muscat–Ibra transect, southeastern Oman Mountains: Journal of Geophysical Research, v. 86, p. 2527–2544.

Huggins, F. E., Virgo, D., and Huckenholz, H. G., 1977, Titanium containing silicate garnets I. The distribution of Al, $Fe^{3+}$, and $Ti^{4+}$ between octahedral and tetrahedral sites: American Mineralogist, v. 62, p. 646–665.

Leblanc, M., and Lbouabi, M., 1988, Native silver mineralization along a rodingite tectonic contact between serpentinite and quartz diorite (Bou Azzer, Morocco): Economic Geology, v. 83, p. 1379–1391.

Le Métour, J., de Gramont, X., and Villey, M., 1986, Geological maps of Masqat and Quryat, sheets NF40-4A, NF40-4D, scale 1:100,000: Muscat, Oman, Ministry of Petroleum and Minerals, Directorate General of Minerals, Sultanate of Oman.

Le Métour, J., Rabu, D., Tegyey, M., Béchennec, F., Beurrier, M., and Villey, M., 1990, Subduction and obduction: Two stages in the Eo-Alpine tectonometamorphic evolution of the Oman Mountains, *in* Robertson, A. H. F., Searle, M. P., and Ries, A. C., eds., The geology and tectonics of the Oman Region: Geological Society, London, Special Publication, v. 49, p. 327–339.

Liou, J. G., Maruyama, S., and Cho, M., 1985, Phase equilibria and mineral parageneses of metabasites in low-grade metamorphism: Mineralogical Magazine, v. 49, p. 321–333.

Meschede, M., 1986, A method of discriminating between different types of Mid-Ocean Ridge basalts and continental tholeiites with the Nb-Zr-Y diagram: Chemical Geology, v. 56, p. 207–218.

Miller, J. M. L., Gregory, R. T., and Gray, D. R., 1998, Geological and geochronological constraints on the exhumation of a high-pressure metamorphic terrane, Oman, *in* Ring, U., Brandon, M. T., Lister, G. T., and Willet, S. D., eds., Exhumation processes: Normal faulting, ductile flow, and erosion: Geological Society of London Special Publication 154, p. 241–260.

Miyashiro, A., and Shido, F., 1975, Tholeiitic and calcalkalic series in relation to the behaviors of vanadium, chromium, and nickel: American Journal of Science, v. 275, p. 265– 277.

O'Hanley, D. S., 1996, Serpentinites, recorders of tectonic and petrological history: Oxford Monographs on Geology and Geophysics, no. 34, 256 p.

Pearce, J. A., and Cann, J. R., 1973, Tectonic setting of basic volcanic rocks determined using trace element analyses: Earth and Planetary Science Letters, v. 19, p. 290–300.

Prinz, M., 1967, Geochemistry of basaltic rocks: Trace elements, *in* Hess, H. H., and Poldervaart, A. A., eds., Basalts: New York, NY, Wiley, p. 271–323.

Prokhor, S. A., 1991, The genesis of nephrite and emplacement of the nephrite-bearing ultramafic complexes of East Sayan: International Geology Review, v. 33, p. 290–300.

Qaiser, M. P., Mansoor, A. S., and Khan, A. H., 1970, Rodingite from Naranji Sar, Dargai ultramafic complex, Malakand, west Pakistan: Mineralogical Magazine, v. 37, p. 736–737.

Rice, J., 1983, Metamorphism of rodingites: Part I. Phase relations in a portion of the system CaO–MgO –$Al_2O_3$–$SiO_2$–$CO_2$–$H_2O$: American Journal of Science, v. 283-A, p. 121–150.

Sanford, R., 1982, Growth of ultramafic reaction zones in greenschist to amphibolite facies metamorphism: American Journal of Science, v. 282, p. 543–616.

Staudigel, H., Plank, T., White, B., and Schmincke, U., 1996, Subduction top to bottom: Geophysical Monographs, v. 96, p. 19–38.

Schandl, E. S., O'Hanley, D. S., and Wicks, F. J., 1989, Rodingites in serpentinized ultramafic rocks of the Abitibi greenstone belt, Ontario: Canadian Mineralogist, v. 27, p. 579–591.

Schandl, E. S., O'Hanley, D. S., Wicks, F. J., and Kyser, K., 1990, Fluid inclusions in rodingite: A geothermometer for serpentinization: Economic Geology, v. 85, p. 1273–1276.

Schiffman, P., and Liou, J. G., 1983, Synthesis of Fe-pumpellyite and its stability relations with epidote: Journal of Metamorphic Geology, v. 1, p. 91–101.

Shervais, J. W., 1982, Ti-V plots and the petrogenesis of modern and ophiolitic lavas: Earth and Planetary Science Letters, v. 59, p. 101–118.

Sun, S.-s. and McDonough, W. F., 1989, Chemical and isotopic systematics of ocean basalts: Implications for mantle composition and processes, *in* Saunders, A. D., and Norry, M. J., eds., Magamatism in the ocean basins: Geological Society of London, Special Publication, v. 42, p. 313–345.

Villey, M., Le Métour, J., and de Gramont, X., 1986, Geological map of Fanjah, sheet NF40-3F, scale 1:100,000. Muscat, Oman, Ministry of Petroleum and Minerals, Directorate General of Minerals, Sultanate of Oman.

Vityk, M. O., and Bodnar, R. J., 1995, Textural evolution of synthetic fluid inclusions in quartz during reequilibration, with applications to tectonic reconstruction: Contributions to Mineralogy and Petrology, v. 119, p. 309–323.

Wares, R. P., and Martin, R. F., 1980, Rodingitization of granite and serpentinite in the Jeffrey mine, Asbestos, Quebec: Canadian Mineralogist, v. 18, p. 231–240.

Wenner, D. B., 1979, Hydrogen, oxygen, and carbon isotopic evidence for the origin of rodingites in serpentinized ultramafic rocks: Geochimica et Cosmochimica Acta, v. 43, p. 603–614.

Wilson, M., 1989, Igneous petrogenesis: London, UK, Unwin Hyman, 466 p.

Winter, J. D., 2001, An introduction to igneous and metamorphic petrology: Upper Saddle River, NJ, Prentice Hall, 697 p.

Zhang, Y., and Franz, J. D., 1987, Determination of the homogenization temperatures and densities of supercritical fluids in the system NaCl-KCl-$CaCl_2$-$H_2O$ using synthetic fluid inclusions: Chemical Geology, v. 64, p. 335–350.